

Discontinuous finite element discretizations for the S_N neutron transport equation in problems with spatially varying cross sections



Peter G. Maginot, Jean C. Ragusa*, Jim E. Morel

Department of Nuclear Engineering, Texas A&M University, 3133 TAMU, College Station, TX 77843, USA

ARTICLE INFO

Article history:

Received 4 February 2014

Received in revised form 26 June 2014

Accepted 27 June 2014

Available online 10 August 2014

Keywords:

Numerical quadrature

Discrete ordinates transport

Discontinuous finite element method

Cross section

Fuel depletion

ABSTRACT

We examine the accuracy of arbitrary degree discontinuous finite element spatial discretizations of the S_N particle transport equations with cross sections that are continuous functions of space. For cell-wise constant cross section problems in purely absorbing materials, it has previously been shown that using arbitrary degree DFEM with quadrature-based mass matrix lumping techniques can result in fully accurate schemes with strictly positive angular flux outflows in 1-D slab geometry. We adapt these quadrature-based, or “self-lumping”, schemes to problems with arbitrarily varying spatial cross sections and incorporate the cross-section spatial dependence into the definition of the mass matrices.

We compare two approaches to deal with the cross-section spatial dependence. The first approach approximates the true cross section as a cell-wise constant that preserves the cell-average cross-section value. The second method uses self-lumping quadrature to evaluate the exact cross section at quadrature points. Regardless of DFEM trial space degree, approximating a spatially varying cross section with a cell-wise constant cross section results in schemes that are at most second-order accurate in space. Additionally, we demonstrate that assuming a cell-wise constant cross section generates interaction rate profiles that have highly non-physical, non-monotonic discontinuities. Using the self-lumping technique to account for cross-section spatial variation with Gauss or Lobatto quadrature yields fully accurate DFEM schemes for problems with spatially varying cross section. Self-lumping schemes that evaluate the cross section at quadrature points do not exhibit non-physical interaction rate profiles. Unfortunately, only a self-lumping linear DFEM with Lobatto quadrature is guaranteed to produce strictly positive angular flux outflow in a pure absorber when accounting for cross-section spatial variation.

Robustness and convergence order comparisons are first carried out using a pure absorber test problem. The cross-section spatial variation is chosen such that an analytical solution can be obtained. Next, we study the spatial effects of isotopic concentration changes during fuel depletion. The depletion problem confirms the accuracy results of the pure-absorber problem.

© 2014 Elsevier Ltd. All rights reserved.

1. Introduction

For many problems of interest to the nuclear science and engineering community, macroscopic cross sections in neutronics and opacities in radiative transfer calculations cannot accurately be described as piecewise constants in space. Cross sections and opacities are functions of continuously varying quantities such as temperature, density, burn-up history, etc. (Stacey, 2001). Examples of simulations that may not be adequately described by cell-wise constant cross sections include nuclear reactor depletion calculations and radiative transfer calculations for high-energy

density physics experiments. However, the majority of neutron transport literature has only considered the case of cell-wise constant cross sections (see Adams, 2001; Lewis and Miller, 1993; Warsa et al., 2004; Wang and Ragusa, 2009). The work of Kavenoky and Lautard (1977) and more recently Santandrea and Bellier (2007) are notable exceptions in neutronics. In Kavenoky and Lautard (1977), continuous cubic finite element diffusion calculations that assume a linearly varying spatial cross section within each mesh cell were compared to results obtained using the same spatial discretization but with the assumption that cross sections are constant in each cell. Similarly, Santandrea and Bellier (2007) compared the results of a linear characteristic scheme that assumes a linearly varying cross section in each spatial cell to those of a linear characteristic scheme that assumes a constant cross section in each cell. Spatial variation of opacity within individual

* Corresponding author.

E-mail addresses: pmaginot@tamu.edu (P.G. Maginot), jean.ragusa@tamu.edu (J.C. Ragusa), morel@tamu.edu (J.E. Morel).

mesh cells for radiative transfer calculations was first proposed by Adams (1997) for “simple” corner balance (SCB) spatial discretization methods and the first SCB computational results for a problem with spatially varying cross section in each cell appeared in Adams and Nowak (1998). The practice of accounting for spatially varying cross sections has become standard in the radiative transfer community for linear spatial discretizations, usually implemented via a vertex-based quadrature evaluation of mass matrix terms (for a finite element discretization), as in Ober and Shadid (2004) and Morel et al. (2007), or through corner balance schemes as originally outlined by Adams.

In this work, we analyze the effects of cross-section spatial dependence on solution accuracy. Our work differs from Kavenoky and Lautard (1977), Santandrea and Bellier (2007), Adams (1997) and Adams and Nowak (1998) by considering a discontinuous finite element (DFEM) spatial discretization of the slab geometry S_N transport equation using arbitrary degree polynomial finite element trial spaces. In addition, like Adams (1997) and Adams and Nowak (1998) we do not make any approximation to the particular spatial shape of the cross-section spatial variation in each cell. We build on the quadrature integration ideas presented in Maginot et al. (2014) and employ a numerical quadrature to evaluate the mass matrix integrals that involve cross sections as a function of space. In general, the quadrature integration of the DFEM interaction term with arbitrary cross sections will not be exact. However, we showed in Maginot et al. (2014) that exact computation of integrals appearing in the DFEM weak form, when cross sections are spatially constant, is not required to achieve high-order accuracy with high-order DFEM approximations. Building on this idea, we investigate the effects of using numerical quadratures to compute DFEM mass matrices, accounting for the spatial variation of cross section in space. As in Maginot et al. (2014), we use self-lumping numerical quadratures (Raviart, 1972; Thomee, 1997), restricting quadrature integration points to the DFEM polynomial interpolation points. Results are compared as a function of DFEM polynomial trial space degree and interpolation point type.

We demonstrate that assuming a piecewise constant cross section in each cell, when the cross section is not cell-wise constant in space, has several undesirable effects. Considering a source-free, purely absorbing medium, we show that DFEM schemes that assume a cell-wise constant cross section are at most second-order accurate for the angular flux solution and limited to at most first-order accuracy for the interaction rate solution, regardless of the DFEM polynomial trial space degree. We also show that assuming a piecewise constant cross section results in a highly discontinuous, non-monotonic spatial interaction rate. This phenomena has likely been present in published numerical results for problems with non-piecewise constant cross section but was not observed previously due to the choice of data presentation.

We then consider schemes that explicitly account for cross-section spatial variation within individual mesh cells. First, the positivity and robustness of different schemes are discussed using a source-free pure absorber problem. Next, we demonstrate that self-lumping schemes that evaluate the DFEM weak form integrals involving cross section with quadrature result in fully accurate schemes for arbitrary degree polynomial DFEM. By fully accurate we mean schemes that achieve the same order of convergence for problems with spatially varying and cell-wise constant cross section, for a given DFEM approximation order. Finally, we study the effects of isotopic spatial variation on DFEM solution accuracy in a fuel depletion problem. The depletion problem shows that self-lumping schemes that explicitly account for both isotopic and cross-section spatial variation are higher-order accurate than schemes that do not account for the spatial variation of both

nuclide density and cross section. Though S_N DFEM methods are not commonly used for reactor physics or depletion problems, ongoing developments, such as the development of scalable DFEM transport sweeps (Adams et al., 2013), may increase the prevalence of DFEM schemes for such calculations (McGraw et al., 2014). Further, we consider a fuel depletion problem primarily as a vehicle to show that self-lumping schemes are accurate and viable for more complex equations that simply steady-state radiation transport calculations.

The remainder of this paper is divided as follows. We derive the weak form DFEM equations with spatially varying cross section in Section 2. In Section 3, we define the different numerical schemes used to solve the DFEM equations. Computational results for pure-absorber test problems are discussed in Section 4. Results for the fuel depletion problem are given in Section 5. Concluding remarks and future work are given in Section 6. A more detailed description of various mesh generating strategies is given in Appendix A and the complete fuel depletion problem description and its solution technique are given in Appendix B.

2. Weak form derivation

We begin by considering the 1-D slab geometry S_N transport equation:

$$\mu_d \frac{d\psi_d(x)}{dx} + \Sigma_t(x)\psi_d(x) = Q_d(x). \quad (1)$$

In Eq. (1), $\psi_d(x)$ is the angular flux [$1/[\text{cm}^2\text{-sec-ster}]$] in μ_d , the directional cosine relative to the x -axis, $\Sigma_t(x)$ is the total interaction cross section [cm^{-1}], and $Q_d(x)$ is the total angular source in the direction of μ_d [$1/[\text{cm}^3\text{-sec-ster}]$]. Q_d includes both scattering and fixed sources. The scalar flux, $\phi(x)$ is defined as:

$$\phi(x) = 2\pi \int_{-1}^1 \psi(x, \mu) d\mu \approx 2\pi \sum_d w_d \psi_d(x). \quad (2)$$

We derive the DFEM equations for a single cell, $x \in [x_L, x_R]$, with the extension to multiple cells being straightforward. A known angular flux, $\psi_{in,d}$, is defined on the incoming face of each cell for a given direction μ_d . $\psi_{in,d}$ comes either from a known boundary condition or from the outflow of the upwind cell. We first transform from the physical geometry to a reference element, $s \in [-1, 1]$, such that:

$$x = \frac{x_L + x_R}{2} + \frac{\Delta x}{2} s \quad (3a)$$

$$dx = \frac{\Delta x}{2} ds, \quad (3b)$$

with $\Delta x = x_R - x_L$. The true angular flux solution, $\psi_d(x)$, is approximated by a Lagrange interpolatory polynomial, $\tilde{\psi}_d(x)$, of degree P :

$$\psi_d(s) \approx \tilde{\psi}_d(s) = \sum_{j=1}^{N_p} \psi_{j,d} B_j(s). \quad (4)$$

The B_j 's are the Lagrange interpolatory functions with interpolatory points s_j ,

$$B_j(s) = \prod_{\substack{k=1 \\ k \neq j}}^{N_p} \frac{s - s_k}{s_j - s_k}, \quad (5)$$

and $N_p = P + 1$. We stress that the interpolatory points, s_j , are not necessarily equally-spaced points. The total angular source, $Q(s, \mu)$, is expanded in a similar fashion:

$$Q_d(s) \approx \tilde{Q}_d(s) = \sum_{j=1}^{N_p} Q_d(s_j) B_j(s). \quad (6)$$

To determine the N_p unknowns of Eq. (4), we follow the standard Galerkin procedure, successively multiplying Eq. (1) by weight function B_i and integrating the result by parts, hence generating N_p moment equations. Inserting our solution representation $\tilde{\psi}_d$, the i -th, exact moment equation is:

$$\mu_d \left[B_i(1) \tilde{\psi}_d(1) - B_i(-1) \tilde{\psi}_d(-1) - \int_{-1}^1 \tilde{\psi}_d(s) \frac{dB_i}{ds} ds \right] + \frac{\Delta x}{2} \int_{-1}^1 \Sigma_t(s) B_i(s) \tilde{\psi}_d(s) ds = \frac{\Delta x}{2} \int_{-1}^1 B_i(s) \tilde{Q}_d(s) ds. \quad (7)$$

We use the upwind approximation to define the angular flux at the cell edges. For $\mu_d > 0$ the angular flux at the cell interfaces is

$$\tilde{\psi}_d(-1) = \psi_{in,d} \quad (8a)$$

$$\tilde{\psi}_d(1) = \sum_{j=1}^{N_p} \psi_{j,d} B_j(1). \quad (8b)$$

Similarly for $\mu_d < 0$:

$$\tilde{\psi}_d(-1) = \sum_{j=1}^{N_p} \psi_{j,d} B_j(-1) \quad (9a)$$

$$\tilde{\psi}_d(1) = \psi_{in,d}. \quad (9b)$$

In Eqs. (8) and (9), $\psi_{in,d}$ is a known angular flux outflow from either the upwind cell or boundary conditions. Using definition of Eqs. (8), and Eq. (7) becomes, for $\mu_d > 0$,

$$\mu_d \left[B_i(1) \left[\sum_{j=1}^{N_p} \psi_{j,d} B_j(1) \right] - B_i(-1) \psi_{in,d} - \int_{-1}^1 \left[\sum_{j=1}^{N_p} \psi_{j,d} B_j(s) \right] \frac{dB_i}{ds} ds \right] + \frac{\Delta x}{2} \int_{-1}^1 \Sigma_t(s) B_i(s) \left[\sum_{j=1}^{N_p} \psi_{j,d} B_j(s) \right] ds = \frac{\Delta x}{2} \int_{-1}^1 B_i(s) \left[\sum_{j=1}^{N_p} Q_d(s_j) B_j(s) \right] ds. \quad (10)$$

For $\mu_d < 0$, using the definition of Eqs. (9) yields:

$$\mu_d \left[B_i(1) \psi_{in,d} - B_i(-1) \left[\sum_{j=1}^{N_p} \psi_{j,d} B_j(-1) \right] - \int_{-1}^1 \left[\sum_{j=1}^{N_p} \psi_{j,d} B_j(s) \right] \frac{dB_i}{ds} ds \right] + \frac{\Delta x}{2} \int_{-1}^1 \Sigma_t(s) B_i(s) \left[\sum_{j=1}^{N_p} \psi_{j,d} B_j(s) \right] ds = \frac{\Delta x}{2} \int_{-1}^1 B_i(s) \left[\sum_{j=1}^{N_p} Q_d(s_j) B_j(s) \right] ds. \quad (11)$$

Considering all N_p moment equations simultaneously, we write both Eqs. (10) and (11) as:

$$\mu_d \mathbf{L} \tilde{\psi}_d - \mu_d \psi_{in,d} \tilde{f} + \frac{\Delta x}{2} \mathbf{R}_{\Sigma_t} \tilde{\psi}_d = \frac{\Delta x}{2} \mathbf{M} \tilde{Q}_d. \quad (12)$$

In Eq. (12) we use the following definitions for the vector of unknowns, $\psi_{j,d}$, and total source components, $Q_{j,d}$:

$$\tilde{\psi}_d = [\psi_{1,d} \dots \psi_{N_p,d}]^T \quad (13)$$

$$\tilde{Q}_d = [Q_d(s_1) \dots Q_d(s_{N_p})]^T. \quad (14)$$

We define the $N_p \times N_p$ reaction matrix, \mathbf{R}_{Σ_t} , as:

$$\mathbf{R}_{\Sigma_t,ij} = \int_{-1}^1 \Sigma_t(s) B_i(s) B_j(s) ds, \quad (15)$$

and the $N_p \times N_p$ mass matrix, \mathbf{M} , as:

$$\mathbf{M}_{ij} = \int_{-1}^1 B_i(s) B_j(s) ds. \quad (16)$$

\tilde{f} is a length N_p column vector. For $\mu_d > 0$:

$$\tilde{f}_i = B_i(-1). \quad (17)$$

For $\mu_d < 0$:

$$\tilde{f}_i = -B_i(1). \quad (18)$$

\mathbf{L} is a $N_p \times N_p$ matrix that we refer to as the gradient operator. When $\mu_d > 0$: \mathbf{L} is:

$$\mathbf{L}_{ij} = B_i(1) B_j(1) - \int_{-1}^1 \frac{dB_i}{ds} B_j ds. \quad (19)$$

For $\mu_d < 0$, \mathbf{L} is:

$$\mathbf{L}_{ij} = -B_i(-1) B_j(-1) - \int_{-1}^1 \frac{dB_i}{ds} B_j ds. \quad (20)$$

3. Numerical schemes

We consider two classes of numerical methods in this paper. The first class uses exact spatial integration to evaluate the integrals that define \mathbf{R}_{Σ_t} , \mathbf{M} , and \mathbf{L} . A second class of methods uses numerical quadrature. Specifically, we limit our discussion of quadrature-based integration to so-called self-lumping methods (Maginot et al., 2014). Self-lumping methods, first discussed in Raviart (1972) and Thomee (1997) for parabolic problems, use a numerical quadrature restricted to the finite element interpolation points, and thus naturally yield diagonal mass matrices. Earlier work for problems with cell-wise constant cross sections (Maginot et al., 2014) demonstrated that, for S_N transport discretized with DFEM, robust and accurate methods can be developed using self-lumping techniques.

A shorthand notation is given in Table 1 for all of the numerical methods considered in this paper and described in detail in the remainder of this section.

3.1. Exact spatial integration

By exact spatial integration, we mean schemes that compute the entries of \mathbf{M} and \mathbf{L} exactly. Here, we achieve this by using equally-spaced interpolation points and employing a Gauss–Legendre quadrature rule (Abramowitz and Stegun, 1972) that exactly integrates the respective integrands. Two schemes use exact spatial integration. One approximates the spatially varying cross section as a cell-wise constant cross section. The other uses the exact cross section when integrating the weak form DFEM quantities involving cross section. The scheme that assumes a cell-wise constant cross section represents the state of the practice in the neutron transport community, while the second scheme represents the ideal scenario for DFEM transport schemes in problems with spatially varying cross sections.

3.1.1. Exact cross section

The exact cross section, exact spatial integration scheme (EXS DFEM) analytically integrates \mathbf{R}_{Σ_t} . Note that since $\Sigma_t(x)$ can be an arbitrary function, analytic integration of \mathbf{R}_{Σ_t} is in general impossible. Likewise, quadrature integration is unlikely to be exact. In our testing of the EXS DFEM scheme, we use a 20-point Gauss–Legendre quadrature to approximately integrate Eq. (15). Alternatively, adaptive quadrature, with a controllable tolerance, may be used such that the quadrature error in evaluating Eq. (15) could be reduced below some small tolerance.

3.1.2. Constant cross section

Historically, neutronics and some radiative transfer calculations have approximated spatially varying cross sections by assuming cell-wise constant cross sections (Adams, 2001; Lewis and Miller, 1993; Warsa et al., 2004; Morel et al., 1996). That is, some evaluation of the true $\Sigma_t(s)$ within a given cell is used to determine a constant value, $\tilde{\Sigma}_t$, within each cell. Under this simplification, \mathbf{R}_{Σ_t} is approximated as:

Table 1

Nomenclature of numerical schemes considered for the pure absorber problem with a spatially exponential cross section.

Interpolation point type	\mathbf{R}_{Σ_t} matrix integration strategy	Gradient operator integration strategy	Method short hand name
Equally-spaced	Exact integration using true $\Sigma_t(x)$	Exactly integrated	EXS DFEM
Equally-spaced	$\Sigma_t(x) \approx \hat{\Sigma}_t$, $\mathbf{R}_{\Sigma_t} \approx \hat{\Sigma}_t \mathbf{M}$ exact integration of \mathbf{M}	Exactly integrated	CXS DFEM
Equally-spaced	Self-lumping via Newton–Cotes quadrature	Approximated with Newton–Cotes quadrature at interpolation points	SLXS Newton–Cotes
Lobatto quadrature	Self-lumping via Lobatto quadrature	Exactly integrated with Lobatto quadrature at interpolation points	SLXS Lobatto
Gauss quadrature	Self-lumping via Gauss quadrature	Exactly integrated with Gauss quadrature at interpolation points	SLXS Gauss

$$\mathbf{R}_{\Sigma_t} = \hat{\Sigma}_t \mathbf{M}. \quad (21)$$

In our test problems, the constant cross-section scheme (CXS DFEM) uses the average of $\Sigma_t(s)$ to generate $\hat{\Sigma}_t$:

$$\hat{\Sigma}_t = \frac{1}{2} \int_{-1}^1 \Sigma_t(s) ds. \quad (22)$$

3.2. Self-lumping quadrature integration

Schemes that are self-lumping evaluate the integrals of Eqs. (15)–(20), using numerical quadrature. By definition, self-lumping schemes create diagonal reaction and mass matrices:

$$\mathbf{R}_{\Sigma_t, ij} = \begin{cases} w_i \Sigma_t(s_i) & i = j \\ 0 & \text{otherwise} \end{cases} \quad (23a)$$

$$\mathbf{M}_{ij} = \begin{cases} w_i & i = j \\ 0 & \text{otherwise} \end{cases} \quad (23b)$$

Though the choice of interpolation points does not affect exact integration schemes, as shown in Maginot et al. (2014), the choice of interpolation points was shown to influence both the robustness and accuracy of self-lumping schemes. We consider equally-spaced closed Newton–Cotes, Lobatto–Gauss–Legendre, and Gauss–Legendre quadratures as interpolation points for self-lumping schemes.

We now briefly highlight the attributes of each self-lumping scheme. Methods are referred to by their shorthand notations, given in Table 1. In a homogeneous, source-free, purely absorbing medium, SLXS Newton–Cotes yields a strictly positive angular flux outflow for all odd degree polynomial trial spaces. SLXS Newton–Cotes in general does not exactly integrate \mathbf{L} or \mathbf{M} . SLXS Lobatto always exactly integrates \mathbf{L} , always approximates \mathbf{M} , and yields strictly positive angular flux outflows in a source-free pure absorber with constant cross section for all odd degree polynomial trial spaces. SLXS Gauss always exactly integrates both \mathbf{L} and \mathbf{M} , and has a strictly positive outflow angular flux for a constant cross section, source-free pure absorber for all even degree polynomial trial

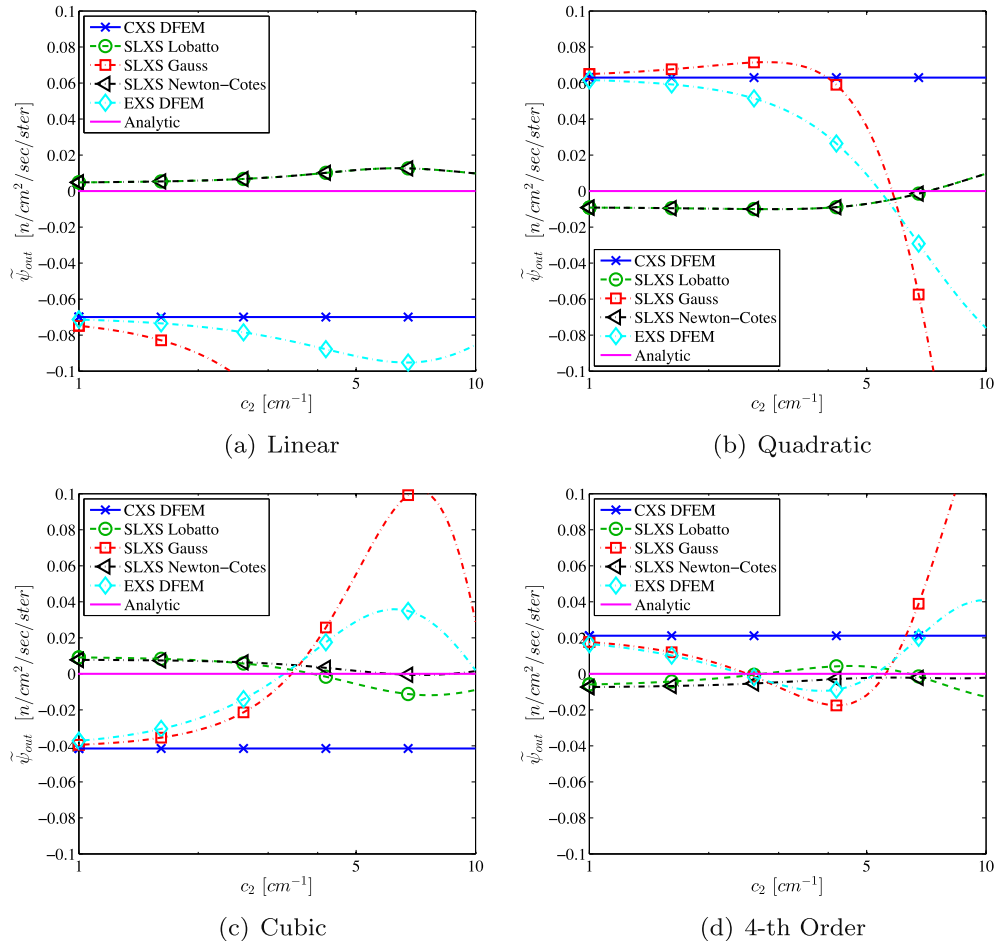


Fig. 1. Numerical outflow from single cell pure absorber with $\Sigma_t(x) = c_1 e^{c_2 x}$, as a function of c_2 with constant optical thickness of twenty MFP, for different degree polynomial trial spaces.

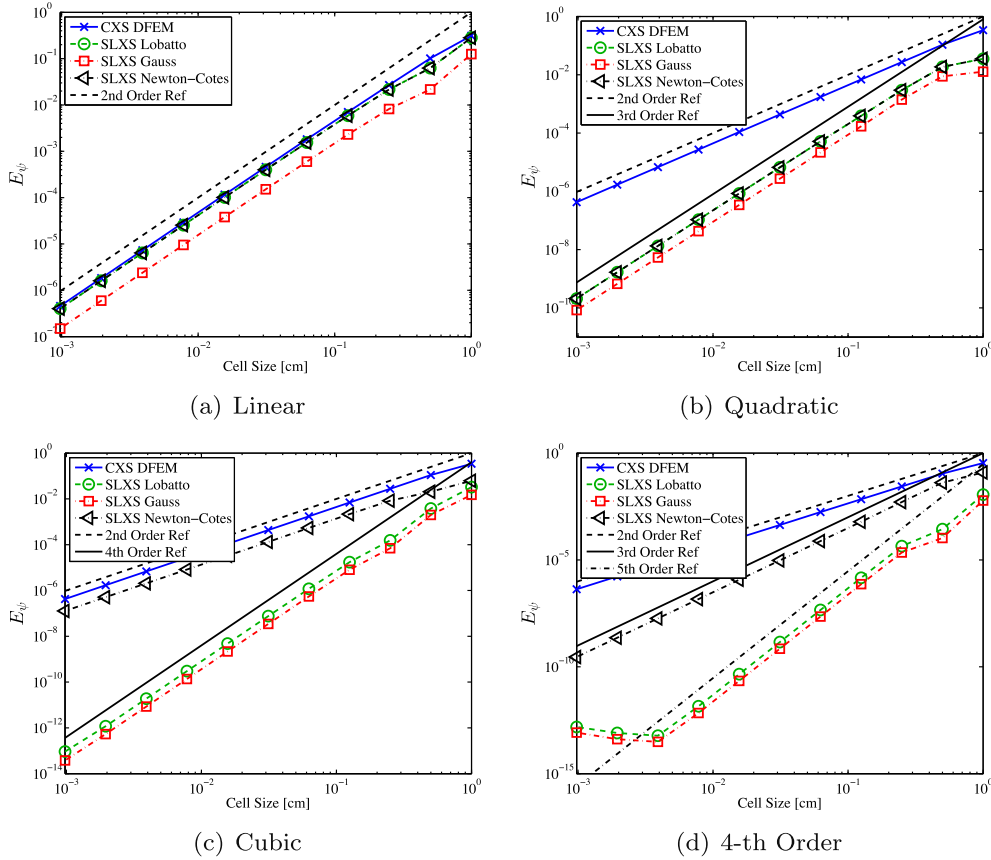


Fig. 2. Convergence of E_ψ for a multiple cell problem as a function of cell size for a pure absorber with exponentially varying cross section, $c_1 = 0.1$ [cm⁻¹], $c_2 = 2 \ln(10)$ [cm⁻¹], and $x \in [0, 1]$ [cm].

spaces. For additional information regarding mass matrix lumping and self-lumping techniques for DFEM S_N transport in homogeneous media, the interested reader is referred to Maginot et al. (2014). We do not expect any self-lumping scheme to exactly integrate \mathbf{R}_{Σ_t} , as the integrand defining \mathbf{R}_{Σ_t} will generally not be a polynomial.

4. Pure absorber numerical results

We first examine the behavior and accuracy of various numerical schemes in a purely absorbing medium with a cross section that varies continuously in space, prior to considering the more complex fuel depletion problem in Section 5. A beam of radiation, $\psi_{in}(\mu_d)$, is incident on the left face of the slab, the right face is a vacuum boundary, $x \in [0, x_R]$, and there are no fixed volumetric sources in the medium. We consider $\Sigma_t(x)$ to be of the form,

$$\Sigma_t(x) = c_1 e^{c_2 x}, \quad (24)$$

with c_1 and c_2 are constants [cm⁻¹], with $c_1 > 0$ and $c_2 \neq 0$. The analytic angular flux solution for a source-free pure absorber with an exponentially varying cross section is:

$$\psi(x, \mu) = \begin{cases} \psi_{in}(\mu) \exp\left[\frac{c_1}{\mu c_2}(1 - e^{c_2 x})\right] & \mu = \mu_d \\ 0 & \text{otherwise} \end{cases} \quad (25)$$

By definition, the outflow angular flux from cell i , $\psi_{out,i}$ is $\psi(x_{i+1/2}, \mu_d)$ and the average angular flux within cell i , $\psi_{A,i}$ as

$$\psi_{A,i} = \frac{1}{\Delta x_i} \int_{x_{i-1/2}}^{x_{i+1/2}} \psi(x, \mu_d) dx, \quad (26)$$

with $\Sigma_t(x)$ defined as in Eq. (24). The analytical average flux value is:

$$\psi_{A,i} = \frac{\psi_{in}(\mu_d)}{\Delta x_i} \exp\left[\frac{c_1}{\mu_d c_2}\right] \left[E_1\left(\frac{c_1 e^{c_2 x_{i+1/2}}}{\mu_d c_2}\right) - E_1\left(\frac{c_1 e^{c_2 x_{i-1/2}}}{\mu_d c_2}\right) \right], \quad (27)$$

with E_1 the exponential integral (Abramowitz and Stegun, 1972).

4.1. Single cell outflow comparisons

The only variable cross-section schemes that yields strictly positive angular outflows in a source-free pure absorber are the SLXS Lobatto and SLXS Newton–Cotes schemes using a linear trial space. For $\mu_d > 0$, consider a source-free, purely absorbing cell with known inflow, $\psi_{in,d}$, of width Δx , and the total cross section at each interpolation point is $\Sigma_{t,j}$. Regardless of the actual functional form of the cross section within the cell, the linear DFEM SLXS Lobatto and SLXS Newton–Cotes schemes' numerical angular flux outflow, $\tilde{\psi}_d(1)$, is:

$$\tilde{\psi}_d(1) = \frac{2\mu_d^2 \psi_{in,d}}{2\mu_d^2 + \Delta x^2 \Sigma_{t,1} \Sigma_{t,2} + \Delta x \mu_d \Sigma_{t,1} + \Delta x \mu_d \Sigma_{t,2}}. \quad (28)$$

Eq. (28) is strictly positive when $\Sigma_t(x) \geq 0$, suggesting that the strictly positive outflow results observed in Maginot et al. (2014) might hold for an arbitrarily varying spatial cross section. However, the results of Maginot et al. (2014) do not hold for higher-order DFEM approximations for spatially dependent cross sections.

To demonstrate that negative cell outflows are possible, we carry out the following test. In Fig. 1, we plot the angular flux outflow of each method as a function of trial space degree, and the parameter c_2 . We hold the total cell optical thickness to 20

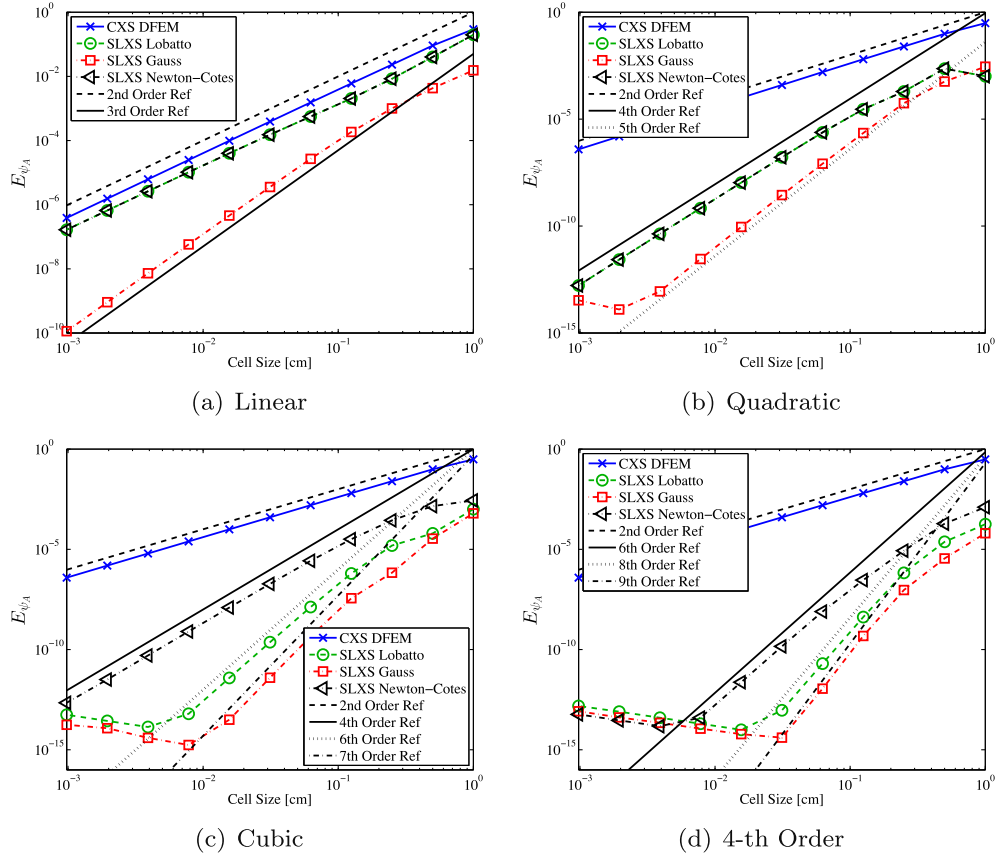


Fig. 3. Convergence of E_{ψ_A} for a multiple cell problem as a function of cell size for a pure absorber with exponentially varying cross section, $c_1 = 0.1 \text{ [cm}^{-1}\text{]}$, $c_2 = 2 \ln(10) \text{ [cm}^{-1}\text{]}$, and $x \in [0, 1 \text{ [cm]]}$.

mean-free-path (MFP), vary $c_2 \in [1, 10]$, fix $x_R = 1$, and $\mu_d = 1$. With an exponential cross section, the cell optical thickness in MFP of a cell with $x \in [0, x_R]$ is:

$$MFP = \int_0^{x_R} \Sigma_t(x) dx = \frac{c_1}{c_2} (e^{c_2 x_R} - 1). \quad (29)$$

To maintain a constant optical thickness in Fig. 1, c_1 is required to be:

$$c_1 = \frac{c_2 MFP}{e^{c_2 x_R} - 1}. \quad (30)$$

Fig. 1 confirms that SLXS Lobatto (and the equivalent SLXS Newton-Cotes scheme) with a linear trial space is the only scheme that explicitly accounts for the spatial variation of cross and maintains a strictly positive angular flux outflow regardless of the shape of $\Sigma_t(x)$. From Fig. 1 we also observe that $\tilde{\psi}_{out}$ varies for every method as a function of the shape of $\Sigma_t(x)$, with the obvious exception of CXS DFEM. Considering that the analytic angular flux outflow is only a function of total cell MFP:

$$\begin{aligned} \psi_{out,i} &= \psi_{in}(\mu_d) \exp \left[- \int_0^{x_{i+1/2}} \Sigma_t(x) dx / \mu_d \right] \\ &= \psi_{in}(\mu_d) \exp [-MFP / \mu_d], \end{aligned} \quad (31)$$

it is unphysical and undesirable that $\tilde{\psi}_{out}$, for the SLXS Gauss, SLXS Lobatto, SLXS Newton-Cotes, and EXS DFEM schemes, depends on the spatial shape of $\Sigma_t(x)$.

4.2. Multiple cell spatial convergence rates

We now consider the order of spatial convergence for the following schemes: CXS DFEM, SLXS Gauss, SLXS Lobatto, and SLXS

Newton-Cotes. Since exact integration of \mathbf{R}_{Σ_t} is generally not feasible, we no longer consider the EXS DFEM scheme. Convergence results of the following angular flux errors as a function of the polynomial approximation order are presented:

$$E_{\psi} = \sqrt{\sum_{i=1}^{N_{cells}} \int_{x_{i-1/2}}^{x_{i+1/2}} (\tilde{\psi}_d(x) - \psi(x, \mu_d))^2 dx} \quad (32a)$$

$$E_{\psi_A} = \sqrt{\sum_{i=1}^{N_{cells}} \Delta x_i (\tilde{\psi}_{A,i} - \psi_{A,i})^2} \quad (32b)$$

$$E_{\psi_{out}} = \sqrt{\sum_{i=1}^{N_{cells}} \Delta x_i (\tilde{\psi}_{out,i} - \psi(x_{i+1/2}, \mu_d))^2}. \quad (32c)$$

In Eqs. (32), Δx_i is the width of cell i , cell i spans $[x_{i-1/2}, x_{i+1/2}]$, $\tilde{\psi}_d(x)$ is the DFEM numerical approximation, $\psi(x, \mu_d)$ is the analytic solution (see Eq. (25)). The problem is spatially discretized using N_{cells} spatial cells of equal width. We approximate the integrals defining the L^2 norm of the angular flux error, E_{ψ} , using a high-order Gauss quadrature set, $(w_{f,q}, s_{f,q})$, with N_{qf} points, such that:

$$\int_{x_{i-1/2}}^{x_{i+1/2}} (\tilde{\psi}(x) - \psi(x, \mu_d))^2 dx \approx \frac{\Delta x_i}{2} \sum_{q=1}^{N_{qf}} w_{f,q} (\tilde{\psi}(s_{f,q}) - \psi(s_{f,q}, \mu_d))^2. \quad (33)$$

For the results that follow, $N_{qf} = 10$. We recall the definitions for the numerical approximations of the cell average angular flux, $\tilde{\psi}_{A,i}$, and the outflow angular flux, $\tilde{\psi}_{out,i}$:

$$\tilde{\psi}_{A,i} = \frac{1}{2} \sum_{j=1}^{N_p} w_j \psi_{ij} \quad (34a)$$

$$\tilde{\psi}_{out,i} = \sum_{j=1}^{N_p} \psi_{ij} B_j(1). \quad (34b)$$

We also consider the convergence of the numerical interaction rate, $\tilde{IR}(x)$ to the true interaction rate $IR(x)$. First, we define the analytic reaction rate for our beam problem:

$$IR(x) = \Sigma_t(x) \psi(x, \mu_d). \quad (35)$$

Similarly, we define a cell average interaction rate as:

$$IR_{A,i} = \frac{1}{\Delta x_i} \int_{x_{i-1/2}}^{x_{i+1/2}} \Sigma_t(x) \psi(x, \mu_d) dx. \quad (36)$$

Defining a point-wise numerical approximation, $\tilde{IR}(x)$, to the analytic interaction rate for the self-lumping schemes presents a unique problem, since only a numerical quadrature is used to approximate the integrand of \mathbf{R} . Quadrature integration only requires point evaluations of $\Sigma_t(x)$, not knowledge of $\Sigma_t(x)$ in between quadrature points. However, for the purpose of plotting the SLXS schemes, we define:

$$\tilde{IR}(s) = \sum_{j=1}^{N_p} B_j(s) \psi_{j,d} \Sigma_t(s_j). \quad (37)$$

It must be emphasized that Eq. (37) is only used for plotting purposes. We approximate the cell average interaction rate in cell i as:

$$\tilde{IR}_{A,i} = \frac{1}{2} \sum_{j=1}^{N_p} w_j \Sigma_t(s_j) \psi_{j,d}. \quad (38)$$

In Eq. (38), $\Sigma_t(s_j) = \hat{\Sigma}_t$ for the CXS DFEM scheme, and $\Sigma_t(s_j)$ is the point evaluation of the true cross section for all other schemes.

We consider two measures to assess the error of the DFEM schemes' approximation of the true interaction rate, $IR(x)$. The first, E_{IR} is an approximation of the L^2 norm of interaction rate error:

$$E_{IR} = \sqrt{\sum_{i=1}^{N_{cells}} \frac{\Delta x_i}{2} \sum_{q=1}^{N_p} w_q \left(IR(s_q) - \tilde{\psi}(s_q, \mu_d) \right)^2}. \quad (39)$$

We reiterate that, for the self-lumping schemes, $\tilde{IR}(s)$ is only truly defined at the DFEM interpolation points. E_{IR_A} measures the convergence of the average interaction rate:

$$E_{IR_A} = \sqrt{\sum_{i=1}^{N_{cells}} \Delta x_i (IR_{A,i} - \tilde{IR}_{A,i})^2}. \quad (40)$$

For our convergence study, we consider a source-free purely absorbing slab with a cross section that varies exponentially in space as in Eq. (24) with $c_1 = 0.1$ and $c_2 = 2 \ln(10)$. A beam of radiation is incident on the left face in the direction of $\mu_d = 1$, vacuum boundary conditions exist on the right face of the slab, and $x \in [0, 1]$. The convergence of the E_{ψ} , E_{ψ_A} , and $E_{\psi_{out}}$ as a function of the choice of numerical scheme and trial space polynomial degree are given in Figs. 2–4, respectively. Convergence of E_{IR} and E_{IR_A} as function of numerical scheme and trial space polynomial degree are given in Figs. 5 and 6. The plateauing of numerical errors for various high-order methods using very small cell sizes in Figs. 2–6, is machine precision. The lines in Figs. 2–6, that extend to values smaller than machine precision are reference lines.

Figs. 2–4, show that, for a linear angular flux trial space, CXS DFEM achieves the same orders of spatial convergence as observed

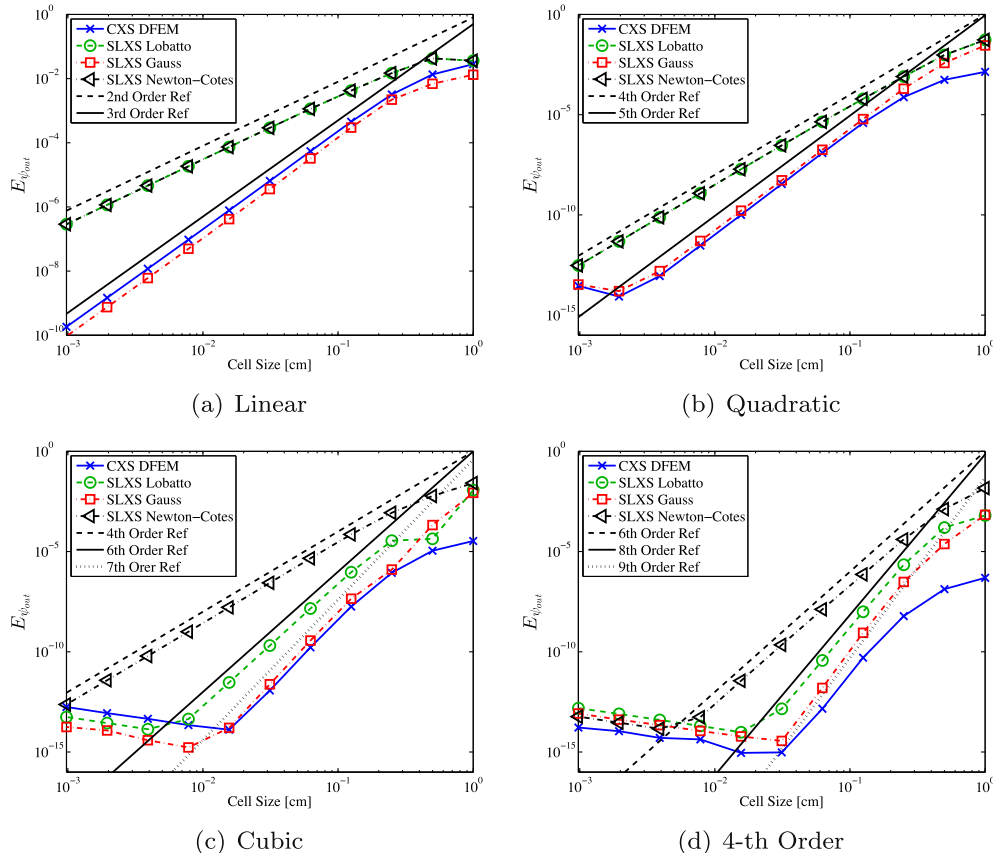


Fig. 4. Convergence of $E_{\psi_{out}}$ for a multiple cell problem as a function of cell size for a pure absorber with exponentially varying cross section, $c_1 = 0.1$ [cm⁻¹], $c_2 = 2 \ln(10)$ [cm⁻¹], and $x \in [0, 1]$ [cm].

with Exact DFEM in Maginot et al. (2014). However, as the degree of the DFEM trial space is increased, the CXS DFEM scheme does not show an increase in the order of the spatial convergence rate of E_ψ and E_{ψ_A} ; the convergence rate of CXS DFEM is limited to at most second order for both E_ψ and E_{ψ_A} , regardless of the trial space polynomial degree. The increase in order of convergence of CXS DFEM for $E_{\psi_{out}}$ as trial space is increased is a result of angular flux outflow in the CXS DFEM discretization being only a function of the cell optical thickness, which is preserved exactly by our definition of $\hat{\Sigma}_t$; see Eq. (22).

Of the self-lumping schemes, SLXS Newton–Cotes is the least accurate. SLXS Newton–Cotes convergence of E_ψ is limited to at most second order for odd degree polynomial trial spaces and third order for even degree trial spaces. Convergence of E_{ψ_A} and $E_{\psi_{out}}$ for the SLXS Newton–Cotes scheme generally increases with an increase in the DFEM polynomial trial space degree, but is only proportional to P .

Both SLXS Lobatto and SLXS Gauss converge E_ψ , E_{ψ_A} , and $E_{\psi_{out}}$ similarly to the study carried out in Maginot et al. (2014) with a spatially constant cross section. The spatial convergence of E_ψ for SLXS Lobatto and SLXS Gauss is order $P + 1$. Though SLXS Lobatto and SLXS Gauss converge with the same order of spatial convergence for E_ψ , SLXS Gauss is more accurate than SLXS Lobatto by a constant. SLXS Gauss converges E_{ψ_A} and $E_{\psi_{out}} \propto 2P + 1$, whereas SLXS Lobatto converges both $\propto 2P$. SLXS Gauss and SLXS Lobatto converge angular flux error quantities for the case of a spatially varying cross section with the same rates of convergence as their constant cross-section analogs did in Maginot et al. (2014). This suggests that exactly integrating the interaction term in the DFEM moment equations is not essential for developing arbitrarily high-order accuracy DFEM schemes for radiation transport.

We observe the detrimental effect of approximating a spatially varying cross section with a constant in each spatial cell when we examine the L_2 convergence results for the interaction rate, E_{IR} , for the CXS DFEM scheme. Regardless of angular flux trial space polynomial degree, CXS DFEM converges E_{IR} to only first order in space. However, the self-lumping schemes exhibit the same trends in converging E_{IR} (in the L^2 -norm sense) as exhibited in converging E_ψ :

- SLXS Lobatto and SLXS Gauss converge E_{IR} with order $P + 1$,
- SLXS Gauss is more accurate than SLXS Lobatto by a constant, and
- SLXS Newton–Cotes converges E_{IR} second order in space for odd degree trial spaces and third order in space for even degree trial spaces.

The convergence results of the cell average interaction rate, E_{IR_A} , shown in Fig. 6, do not behave as intuitively. Given the poor performance of CXS DFEM in converging E_{IR} , one would expect that CXS DFEM would converge E_{IR_A} poorly as well. However, this is not the case and CXS DFEM converges E_{IR_A} with the same order of convergence as the best performing self-lumping scheme considered. CXS DFEM converges E_{IR_A} with a high-order of accuracy because of the locally conservative properties of DFEM approximations, that is:

Particles Into Cell – Particles Out of Cell

$$= \text{Total Interactions in Cell.} \quad (41)$$

As shown in Fig. 4, CXS DFEM converges the quantities on the left hand side of Eq. (41) with the same order of accuracy as any self-lumping scheme considered; CXS DFEM is at least as accurate

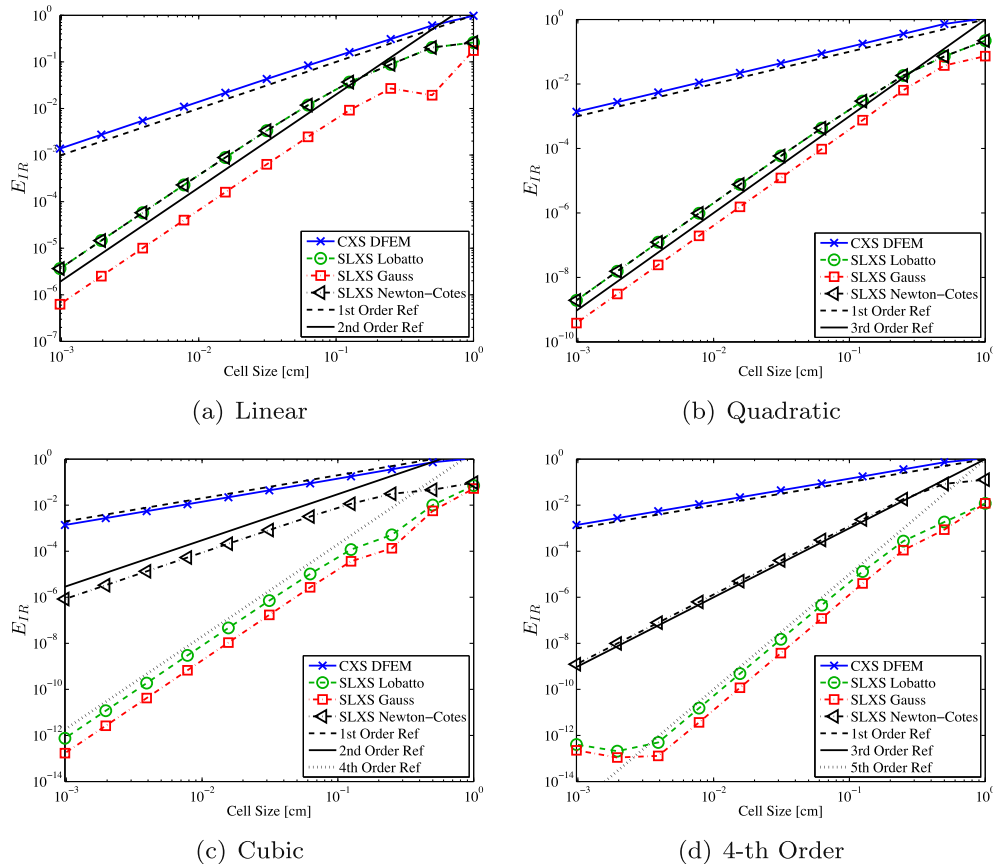


Fig. 5. Convergence of E_{IR} for a multiple cell problem as a function of cell size for a pure absorber with exponentially varying cross section, $c_1 = 0.1 \text{ [cm}^{-1}\text{]}$, $c_2 = 2 \ln(10) \text{ [cm}^{-1}\text{]}$, and $x \in [0, 1 \text{ [cm]]}$.

in calculating the particles into a cell (outflow from the previous cell) and out of the cell (outflow from the current cell) as any other scheme considered. Since Eq. (41) holds regardless of the numerical scheme considered, it follows that CXS DFEM converges E_{IR_A} , the term in the right hand side of Eq. (41) summed over all cells, with the maximum order of convergence displayed by any of the DFEM schemes we consider here. Fig. 6 validates this conclusion. CXS DFEM and SLXS Gauss exhibit the highest order of spatial convergence, converging E_{IR_A} with order $\propto 2P + 1$. SLXS Newton–Cotes and SLXS Lobatto converge E_{IR_A} with the same orders of convergence

each method exhibits in converging E_{ψ_A} for this problem with SLXS Lobatto converging $\propto 2P$ and SLXS Newton–Cotes $\propto P$.

4.3. Consequences of assuming a cell-wise constant cross section

To understand the poor convergence of point-wise error in angular flux and interaction rate, E_{ψ} and E_{IR} , associated with CXS DFEM we now examine more closely the CXS DFEM spatial approximations to $\psi(x, \mu_d)$ and $IR(x)$. We again consider a pure absorber with total absorption cross section that varies exponentially in

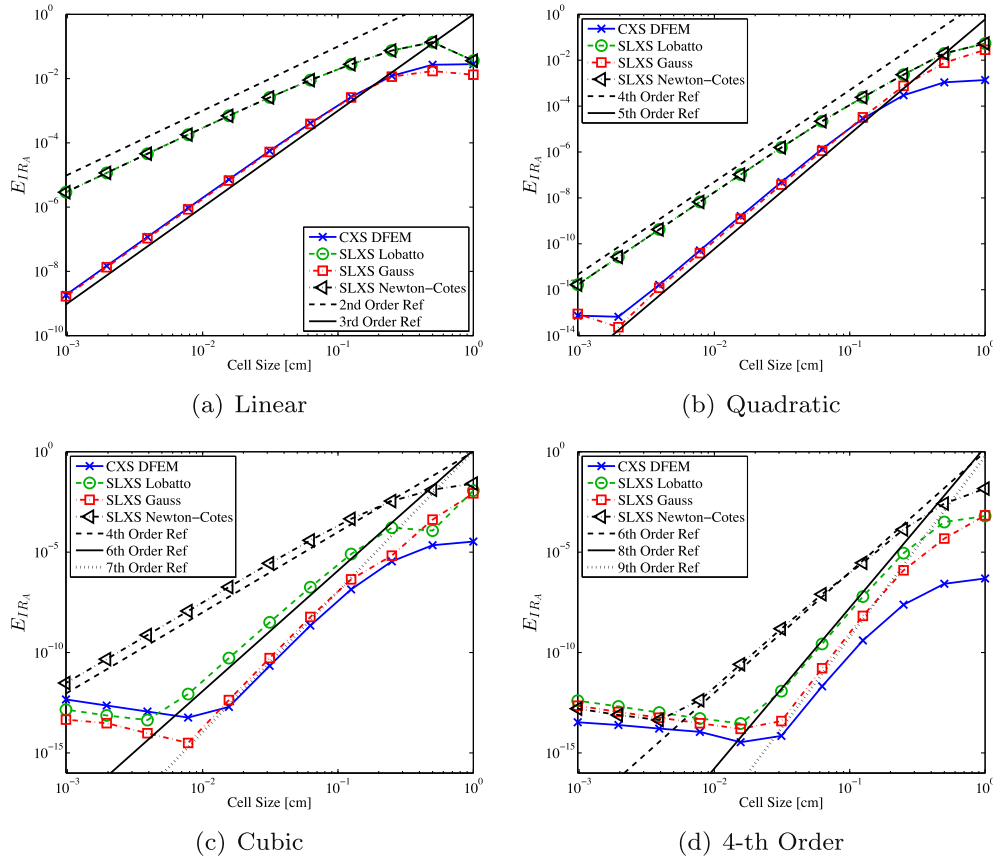


Fig. 6. Convergence of E_{IR_A} for a multiple cell problem as a function of cell size for a pure absorber with exponentially varying cross section, $c_1 = 0.1 \text{ [cm}^{-1}\text{]}$, $c_2 = 2 \ln(10) \text{ [cm}^{-1}\text{]}$, and $x \in [0, 1 \text{ [cm]}]$.

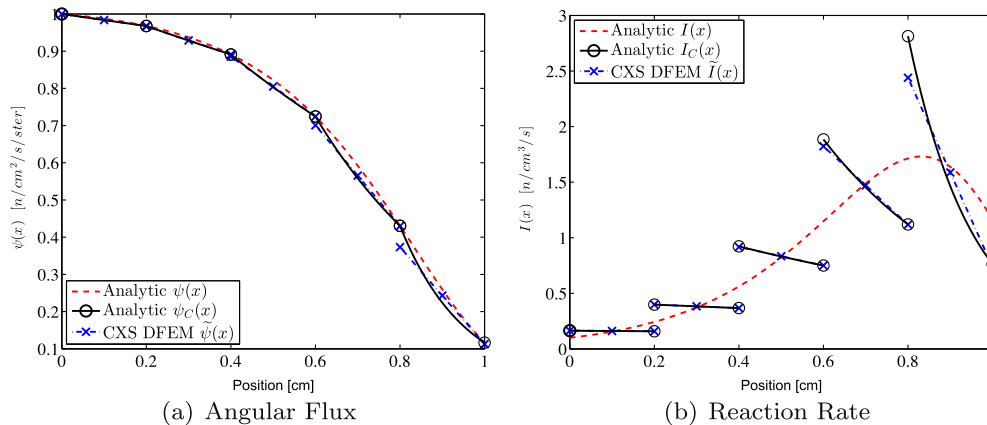


Fig. 7. Plots of the analytic $\psi(x)$ and $IR(x)$ and the CXS DFEM $\tilde{\psi}(x)$ and $\tilde{IR}(x)$ for the pure absorber with exponential cross section. Also shown are the analytic $\psi_C(x)$ and $IR_C(x)$ solutions.

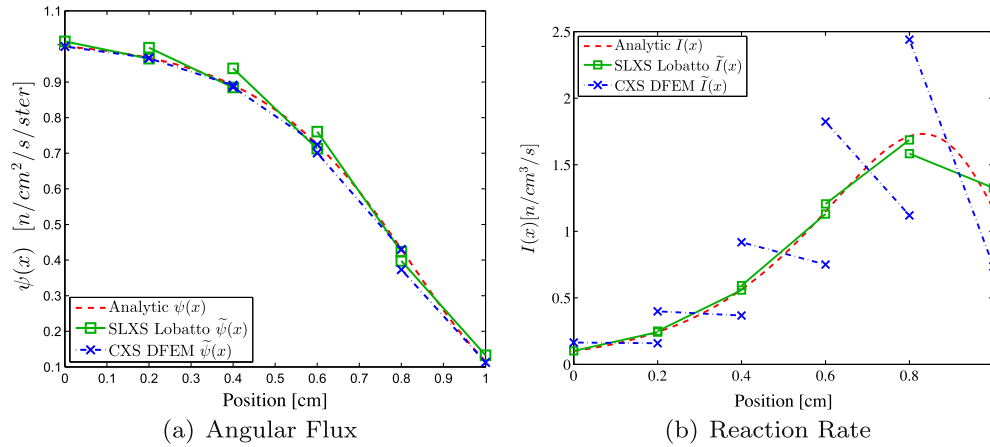


Fig. 8. Plot of the linear trial space SLXS Lobatto and CXS DFEM approximations $\tilde{\psi}(x)$ and $\tilde{I}(x)$ for the pure absorber problem with exponentially varying cross section.

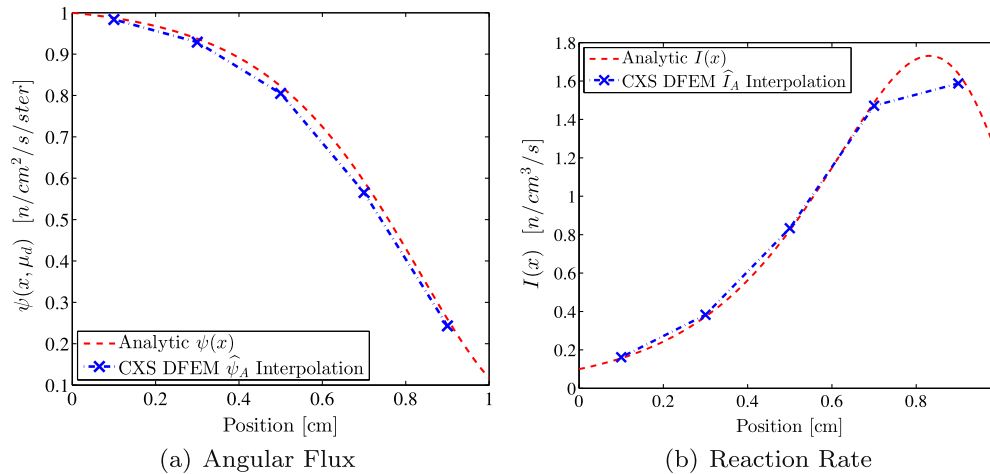


Fig. 9. Plot of the CXS DFEM cell average angular fluxes and interaction rates at cell centers with linear interpolation for a pure absorber with a spatially varying cross section.

space with $c_1 = 0.1$, and $c_2 = 2 \ln(10)$. A beam of radiation is incident on the left face in the direction of $\mu_d = 1$, vacuum boundary conditions are applied on the right face of the slab, and $x \in [0, 1]$.

In Fig. 7, we plot the exact $\psi(x)$ and $IR(x)$, as well as their CXS DFEM numerical approximations, $\tilde{\psi}(x)$ and $\tilde{I}(x)$, using $N_{\text{cells}} = 5$, and $\tilde{\Sigma}_{t,i}$ as defined in Eq. (22). Additionally, we plot the analytic angular flux and reaction rate one would obtain if the cell average cross section, $\tilde{\Sigma}_{t,i}$, had been used instead of the true $\Sigma_t(x)$. We refer to these analytic solutions as $\psi_c(x)$ and $IR_c(x)$.

Since CXS DFEM is a discontinuous scheme, some discontinuity is expected in the plots of $\tilde{\psi}$ and \tilde{I} in Fig. 7. However, the discontinuities present in $\tilde{I}(x)$ of Fig. 7 are highly disconcerting. The analytic $IR(x)$ is smooth and does not vary rapidly within individual mesh cells, yet there are significant, non-monotonic discontinuities in the CXS DFEM interaction rate solution to the pure absorber problem with exponentially varying cross section. The noticeably poor behavior of $\tilde{I}(x)$ in Fig. 7 is inherent to the assumption of a cell-wise constant cross section. This is clearly visible in Fig. 7 when $\psi(x)$ and $IR(x)$, calculated assuming a spatially varying cross section, are compared to the analytic solutions assuming a cell average cross section, $\psi_c(x)$ and $IR_c(x)$. Fig. 7 does not suggest that linear DFEM is unsuitable for use in problems with spatially varying cross sections. Rather, comparing the CXS DFEM $\tilde{\psi}(x)$ and $\tilde{I}(x)$ to $\psi_c(x)$ and $IR_c(x)$ in Fig. 7a, we see that CXS DFEM is very accurate when the problem is assumed to have piece-wise constant, cell averaged cross sections.

Given the poor accuracy of CXS DFEM in approximating the true $\psi(x)$ and $IR(x)$, consider $\tilde{\psi}(x)$ and $\tilde{I}(x)$ obtained with SLXS Lobatto using a linear DFEM trial space and five spatial cells, shown in Fig. 8, for the same problem. In Fig. 8(a), the differences between the angular flux solutions obtained using (1) a cell-wise constant cross section (CXS DFEM) and (2) evaluating cross section values at quadrature points (SLXS Lobatto) are small. This is not the case when comparing the different approximations to the interaction rate, $\tilde{I}(x)$, in Fig. 8(b). Though there are discontinuities in the SLXS Lobatto $\tilde{I}(x)$, the discontinuities are smaller and the SLXS Lobatto $\tilde{I}(x)$ is monotonic unlike the CXS DFEM $\tilde{I}(x)$. The SLXS Lobatto $\tilde{I}(x)$ is clearly more accurate than the CXS DFEM $\tilde{I}(x)$. In this problem, there are two possible sources of error that could cause a DFEM to be inaccurate: inexact matrix evaluation and not incorporating cross-section spatial variation into the scheme. By definition, CXS DFEM exactly integrates the mass matrix, and we showed in Maginot et al. (2014) that schemes which exactly integrate the mass matrix are more accurate than schemes that only approximately integrate the mass matrix, like SLXS Lobatto. Thus, the poor accuracy of CXS DFEM relative to SLXS Lobatto is entirely caused by the approximation of a spatially varying cross section with a cell-wise constant value.

The “blading” in $\tilde{I}(x)$ has not previously been reported in the radiation transport literature. We are likely not the first to have generated these large, non-monotonic discontinuities. In fact, we

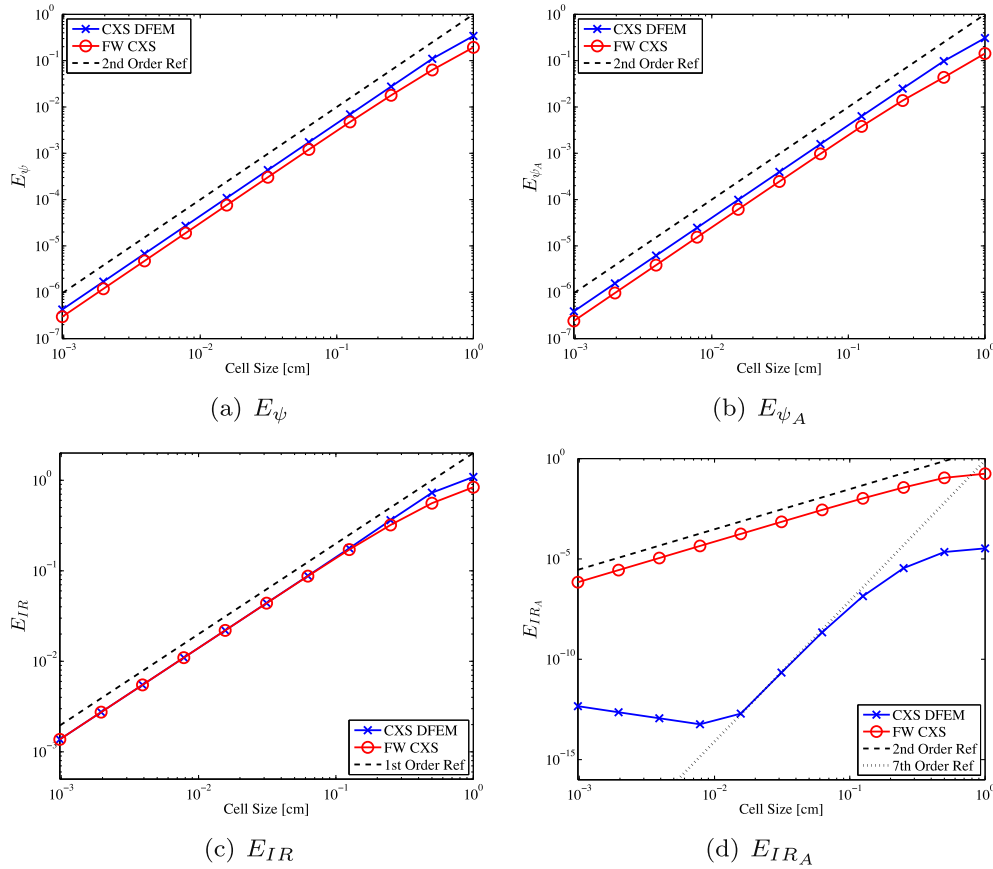


Fig. 10. Accuracy comparison of flux weighted constant cross section scheme (FW CXS) to volume averaged cross section scheme (CXS DFEM) with a cubic angular flux trial space.

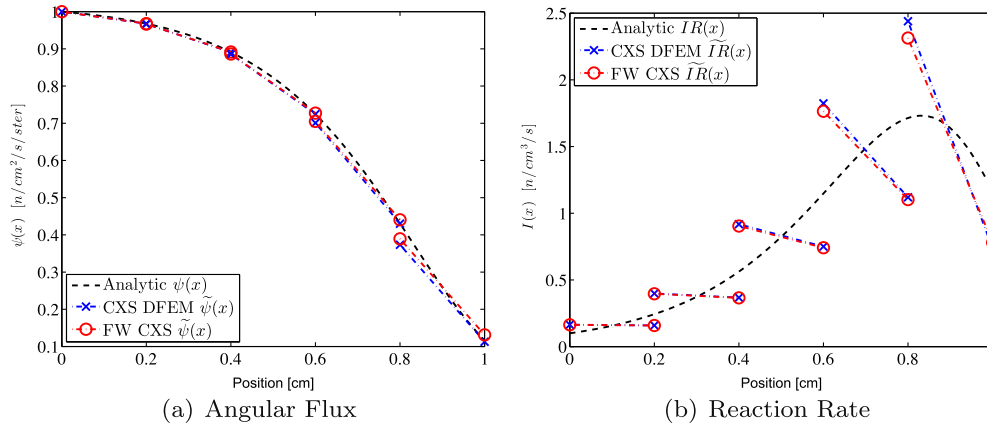


Fig. 11. Plot of the linear trial space FW CXS and CXS DFEM approximations $\tilde{\psi}(x)$ and $\tilde{I}_R(x)$ for the pure absorber problem.

believe that blading has frequently been present in DFEM radiation transport simulations and literature, but has likely gone unnoticed due to the prevalence of linear DFEM and simplified data visualization using cell midpoint values. Consider Fig. 9(a) and (b) that linearly interpolate between $\tilde{\psi}_{A,i}$ and $\tilde{I}_{R,i}$ plotted at cell centers. While Fig. 9(a) is visually indistinguishable from Fig. 7(a), the blading of $\tilde{I}_R(x)$ present in Fig. 7(b) is not at all visually present in Fig. 9(b).

Interaction rate terms are present in other radiation transport physics. In particular, we think of the radiative transfer analog to the neutronics interaction rate, absorption rate density.

4.4. Flux-weighting versus volume-averaged cross sections

In our results thus far, we have only considered volume-averaged cell-wise cross sections (the CXS DFEM scheme).

Table 2

Shorthand notation of different cell spacing schemes.

Spacing label	Spacing type
EQUAL	Equally-spaced cells
MFP	Constant optical thickness cells
LOG	Logarithmically spaced cells

However, in reactor physics problems, a flux-weighted cross section is often used to generate spatially averaged cross sections (Bell and Glasstone, 1970). We now introduce the flux-weighted cell-wise constant cross section scheme (FW CXS), which differs from the CXS DFEM scheme only by how $\hat{\Sigma}$ is defined in each cell:

$$\hat{\Sigma}_i = \frac{\int_{x_{i-1/2}}^{x_{i+1/2}} \Sigma(x) \psi(x, \mu_d) dx}{\int_{x_{i-1/2}}^{x_{i+1/2}} \psi(x, \mu_d) dx}. \quad (42)$$

In practice, flux-weighting is often done using the scalar flux in order not to have angle-dependent total cross section. However, for the beam problem considered here, $\psi(x, \mu_d)$ is proportional to the scalar flux.

We first compare the accuracy of FW CXS versus volume-averaged CXS DFEM for a cubic DFEM trial space, as shown in Fig. 10. Fig. 10 shows that FW CXS scheme is more accurate than CXS DFEM when comparing E_ψ , E_{ψ_A} and, at low resolutions, for E_{IR} . However, though designed to preserve cell average interaction rates, FW CXS scheme is not only less accurate than CXS DFEM in calculating cell average interaction rates, it converges at most second order in space, whereas a volume-averaged cross section converges $\propto 2P + 1$ for the pure absorber problem.

Finally, we consider the $\hat{\psi}_d(x)$ and $\hat{IR}(x)$ solution representations of the FW CXS scheme. In Fig. 11 it is clear that while the FW CXS and CXS DFEM schemes calculate slightly different solution representations, the FW CXS scheme exhibits the same interaction rate blading phenomena as the CXS DFEM scheme, reiterating that blading is a result of approximating a spatially varying cross section

with as a cell-wise constant. The choice of cell-wise cross section does not eliminate blading.

4.5. Effects of mesh spacing

In practice, computational domains are not necessarily discretized with uniform grids; rather cells are concentrated in regions where the solution is known or assumed to vary rapidly. For the pure absorber problem, we compare two alternative methods of mesh spacing (logarithmic grids and equal optical thickness grids, see Table 2), to the results obtained with equally-spaced mesh cells. A more complete discussion of how the different meshes are generated and how they affect the computational results is given in Appendix A. The important results from Figs. 12 and 13 are summarized here:

1. mesh spacing does not affect asymptotic order of convergence,
2. accuracy in calculating certain quantities of interest (point-wise and cell averaged reaction rates) is improved with alternative meshing strategies at low resolution.

5. Fuel depletion results

We consider a fuel depletion problem to illustrate that self-lumping DFEM schemes remain accurate for more complex physics than simply a purely absorbing medium. The depletion method we use [time stepping scheme, time step size, etc.] is chosen for its simplicity, not for its fidelity relative to state-of-the art depletion

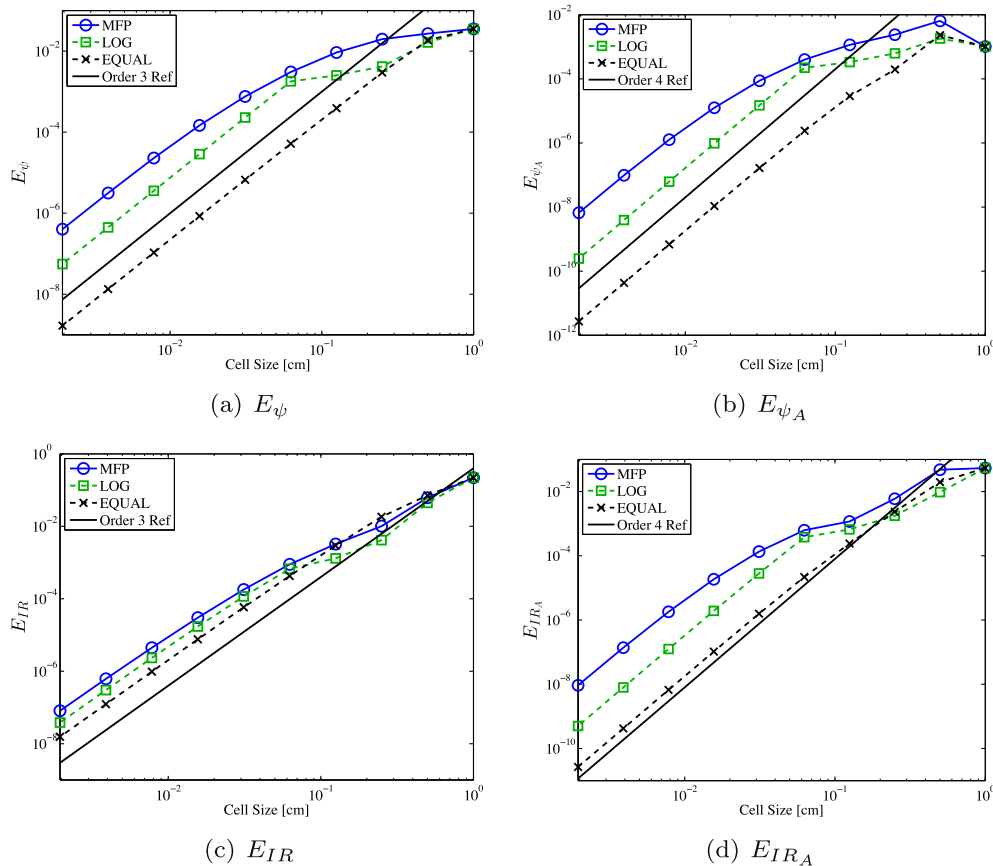


Fig. 12. Asymptotic convergence of the SLXS Lobatto scheme using a quadratic trial space, for different mesh spacing methodologies.

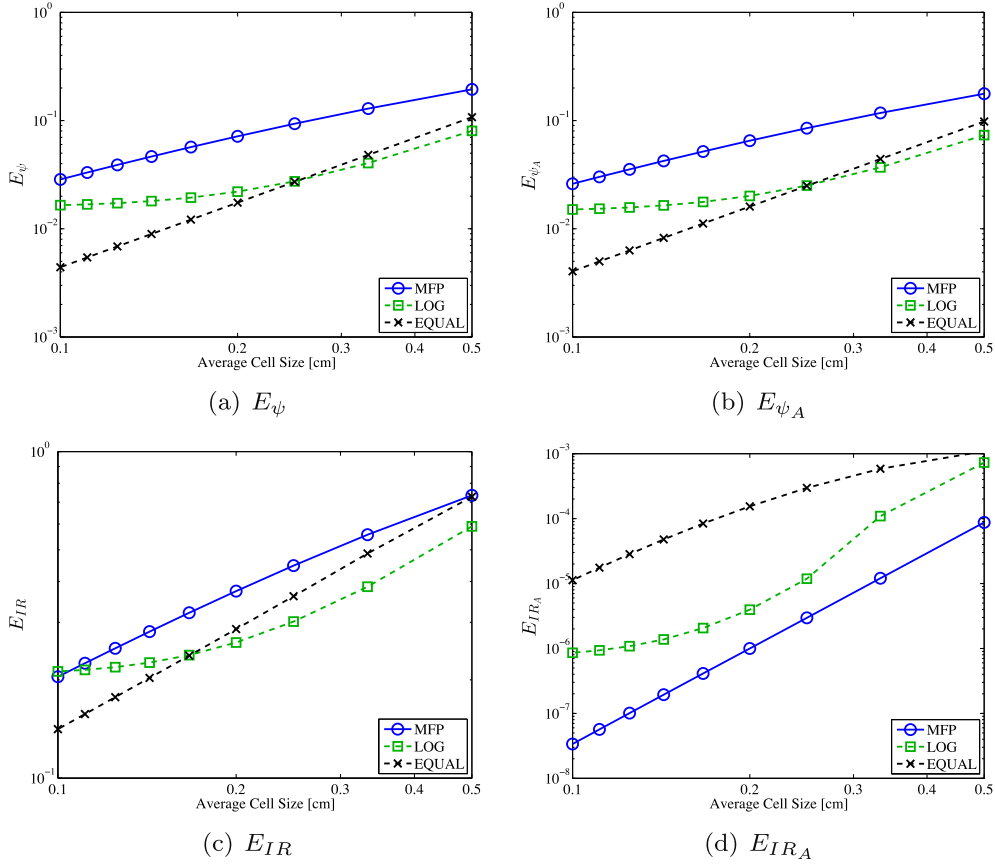


Fig. 13. Errors associated with CXS DFEM using a quadratic trial space for different mesh spacing methodologies, at low resolutions.

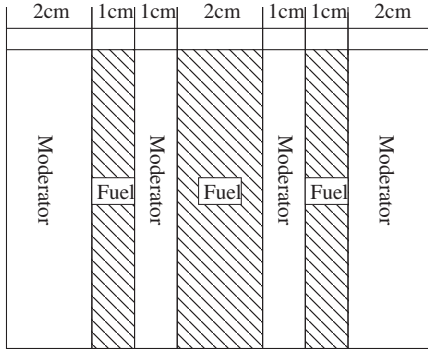


Fig. 14. Depletion problem fuel/moderator lattice.

methodologies. Our goal is to assess the accuracy of *spatial discretization* methods for problems with spatially varying cross sections, not to propose a new depletion method. However, we stress that self-lumping methods can be implemented with any time depletion method or time stepping scheme since implementation of self-lumping only requires changes pertaining to the spatial discretization. Indeed, a depletion scheme that uses a cell-wise constant cross section at a given time t^* computes the interaction matrix as

$$\mathbf{R}_{\Sigma^*} = \hat{\Sigma}^* \mathbf{M}. \quad (43)$$

With self-lumping, one would only need to use the space-dependent cross section at the same time to obtain

$$(\mathbf{R}_{\Sigma^*})_{ij} = \begin{cases} w_i \Sigma^*(s_i) & i = j \\ 0 & \text{otherwise} \end{cases}. \quad (44)$$

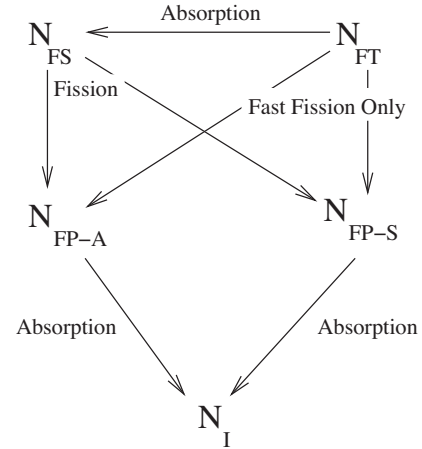


Fig. 15. Depletion problem possible transmutation paths and mechanisms.

The complete definition and detailed solution methodology for the fuel depletion problem are provided in [Appendix B](#). The 1-D geometry of fuel and moderator layers is shown in [Fig. 14](#). The fresh fuel composition is spatially uniform in each fuel region. As the fuel depletes, its isotopic concentrations will deviate from being cell-wise constant. We track five nuclide densities in each fuel region:

1. fissile (N_{FS}),
2. fertile (N_{FT}),
3. parasitic absorber fission product (N_{FP-A}),
4. scattering fission product (N_{FP-S}), and
5. inert (N_I).

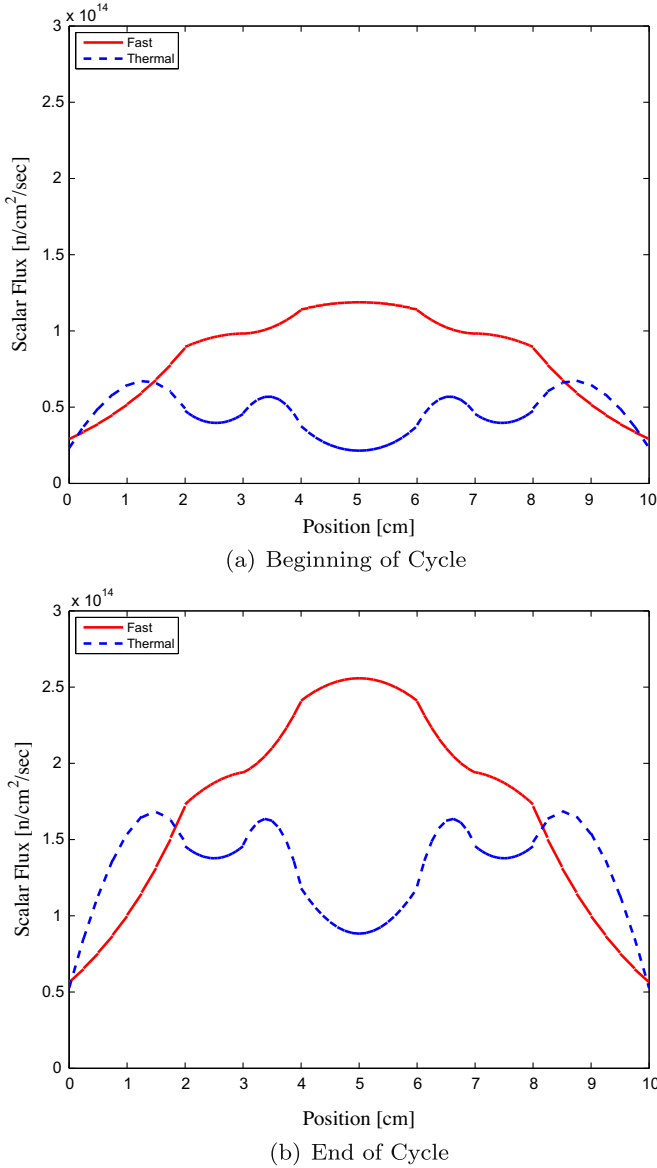


Fig. 16. Example normalized scalar flux profiles at beginning and end of fuel burn-up cycle.

Each fuel region is initially loaded only with fissile and fertile nuclides. We assume no radioactive decay. All possible transmutation paths are shown in Fig. 15. Vacuum boundary conditions are imposed on both sides of the slab. We normalize reactor scalar flux values so that the reactor produces a constant fission power level of 2000 [W] for the duration of the burn-up cycle. The burn-up cycle length consists of 600 full-power days and we use a time step of 10 days to update the scalar fluxes. Typical beginning-of-cycle and end-of-cycle scalar flux profiles are shown in Fig. 16. We consider three numerical methods,

1. SL Full: expand both the angular flux and nuclide densities in a degree P DFEM trial space, compute \mathbf{R}_{Σ_t} and \mathbf{M} as in Eq. (23);
2. SL Collapse: expand both the angular flux and nuclide density in a degree P DFEM trial space, but compute \mathbf{R}_{Σ_t} assuming a cell-wise constant cross section and self-lumping quadrature to approximate \mathbf{M} ; and
3. AD DFEM: expand the angular flux in a P degree polynomial DFEM trial space, track only the cell average nuclide

density, exactly integrate \mathbf{M} , and use a cell-wise average cross section as in Eq. (21) to compute \mathbf{R}_{Σ_t} .

The SL Full and SL Collapse schemes use a Lobatto quadrature for the DFEM interpolation points for odd degree polynomial trial spaces and a Gauss quadrature for interpolation points when the DFEM trial space is an even degree polynomial. The choice of interpolation type does not affect the numerical results of the AD DFEM scheme. SL Collapse expands the nuclide density in a P degree polynomial for the purpose of advancing the nuclide production/destruction equations but uses a cell-wise average cross section for updating the scalar flux. Given the DFEM approximation, $\tilde{N}(x)$, to the true nuclide density, $N(x)$, SL Collapse calculates $\tilde{\Sigma}_t$ for each cell, using the cell average of $\tilde{N}(x)$ to generate an average cross section for each cell to update the scalar flux.

Since an analytic solution to this depletion problem is not available we employ a fine spatial mesh to obtain the reference solution. We use a fine mesh of 10,240 cells and the SL Full scheme with a quartic polynomial trial space as our reference numerical solution. We present L_2 spatial error measures for

1. the total scalar flux (E_ϕ),
2. the fissile nuclide density ($E_{N_{FS}}$),
3. the fertile nuclide density ($E_{N_{FT}}$), and
4. the parasitic absorber fission product ($E_{N_{FP-A}}$).

To allow for easier comparison, we normalize each error to the reference solution quantity. We define E_ϕ as:

$$E_\phi = \frac{\sqrt{\sum_{g=1}^2 \sum_{i=1}^{N_{ref}} \frac{\Delta x_i}{2} \sum_{q=1}^{N_{gf}} w_q \left(\tilde{\phi}_{ref,i,g}(s_q) - \tilde{\phi}_{num,i,g}(s_q) \right)^2}}{\sqrt{\sum_{g=1}^2 \sum_{i=1}^{N_{ref}} \frac{\Delta x_i}{2} \sum_{q=1}^{N_{gf}} w_q \tilde{\phi}_{ref,i,g}(s_q)^2}}, \quad (45)$$

where N_{ref} is the number of reference cells, $\tilde{\phi}_{ref,i,g}(s)$ is the reference solution group g scalar flux in cell i , and $\tilde{\phi}_{num,i,g}(s)$ is the coarse mesh numerical scheme's approximation of the group g scalar flux in cell i . Error measures for N_{FS} , N_{FT} , and N_{FP-A} are derived similarly. Convergence of E_ϕ , $E_{N_{FS}}$, $E_{N_{FT}}$, and $E_{N_{FP-A}}$ are shown respectively in Figs. 17–20.

Fig. 17 re-emphasizes two key results observed in the case of a pure absorber. First, when employing cell-wise constant cross sections, angular/scalar flux convergence is at most second order in space, regardless of the DFEM trial space polynomial degree. Second, exact integration of the interaction terms in the DFEM moment equations is not required to achieve high-order accuracy. In the depletion term, the DFEM interaction term is a degree $3P$ polynomial, and self-lumping schemes using Gauss or Lobatto quadrature only integrate $2P + 1$ and $2P - 1$ degree polynomials, respectively.

Examining the spatial convergence in nuclide densities, we make several observations. First, we note that the AD DFEM scheme (cell-wise average cross section, cell average nuclide density) achieves at most first-order convergence for all spatial nuclide density errors, regardless of the angular flux trial space degree. The AD DFEM scheme is limited to at most first-order convergence of the error in the spatial distribution of nuclides because the scalar flux is updated using only a cell-wise average cross section and only the cell average nuclide density is tracked. Second, though the SL Collapse scheme expands nuclide density in a P degree polynomial DFEM trial space, it achieves at most second-order L^2 convergence of the error in nuclides spatial distribution, for all trial space polynomial degrees. SL Collapse is limited to at most second-order convergence of the spatial nuclide density solely because the scheme assumes a constant cross section in each cell when updating the scalar flux. The respective first-order and second-order convergence of the error in nuclide spatial distribution of the AD

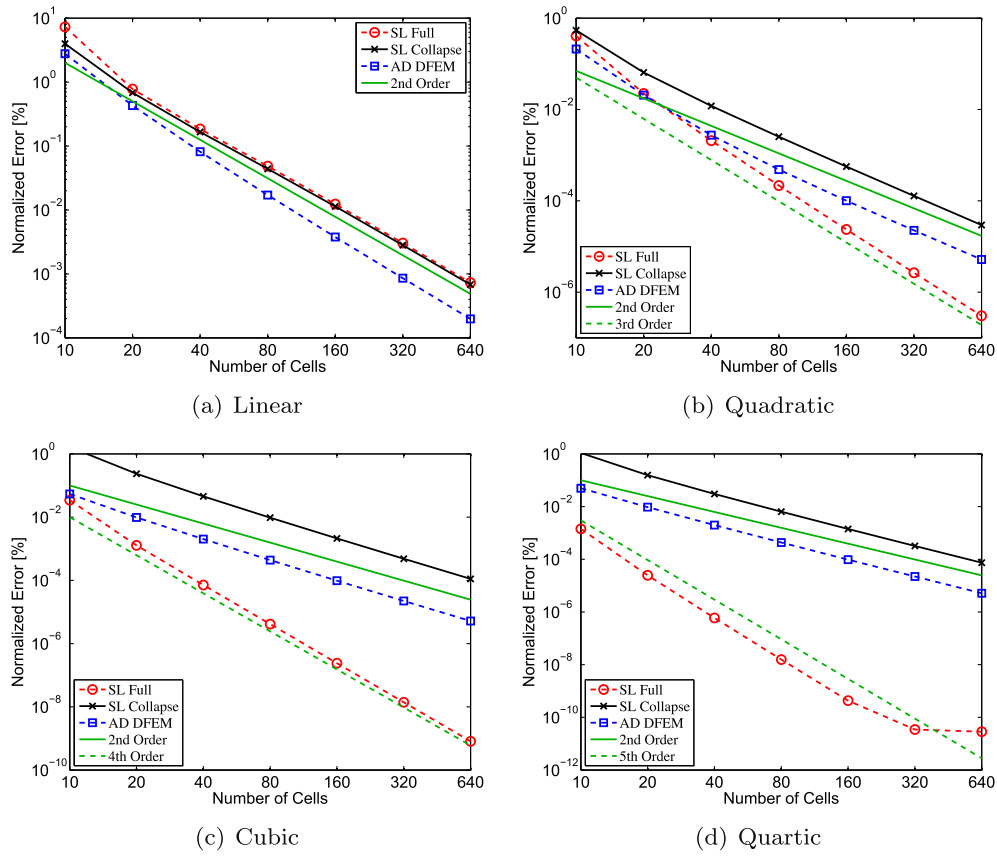


Fig. 17. Normalized total scalar flux error, E_ϕ , for the depletion problem at end of cycle, as a function of angular flux trial space degree.

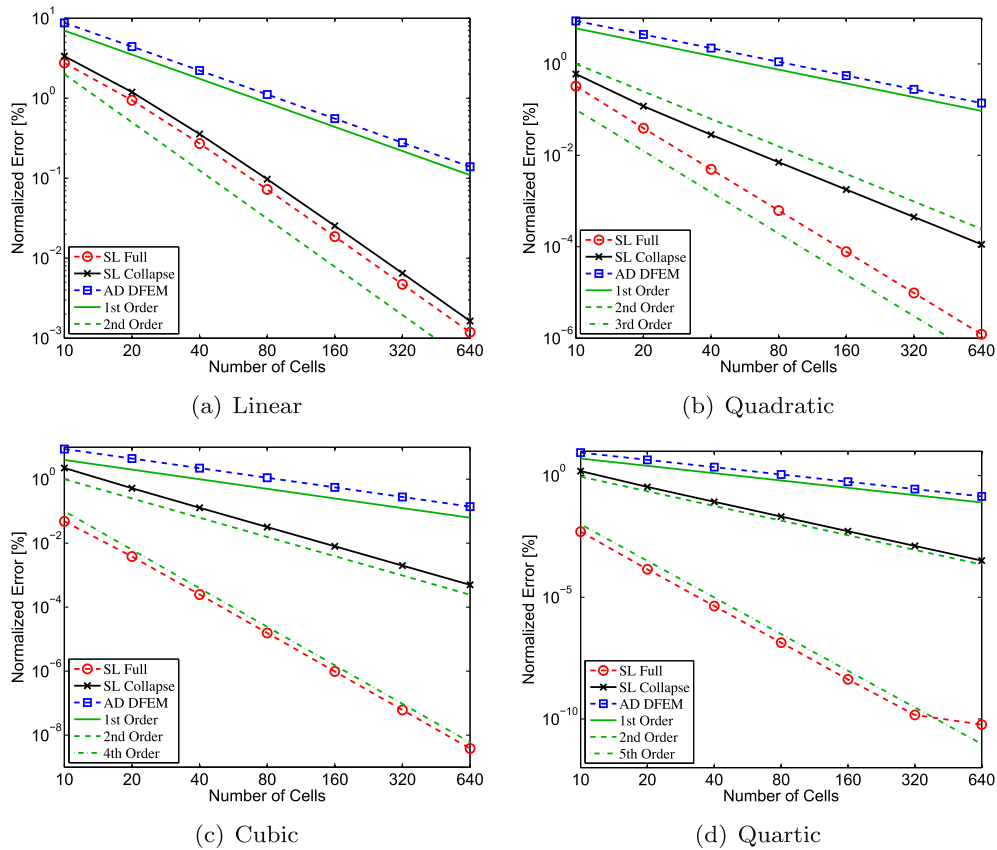


Fig. 18. Normalized fissile nuclide density error, E_{NIS} , for the depletion problem at end of cycle, as a function of angular flux trial space degree.

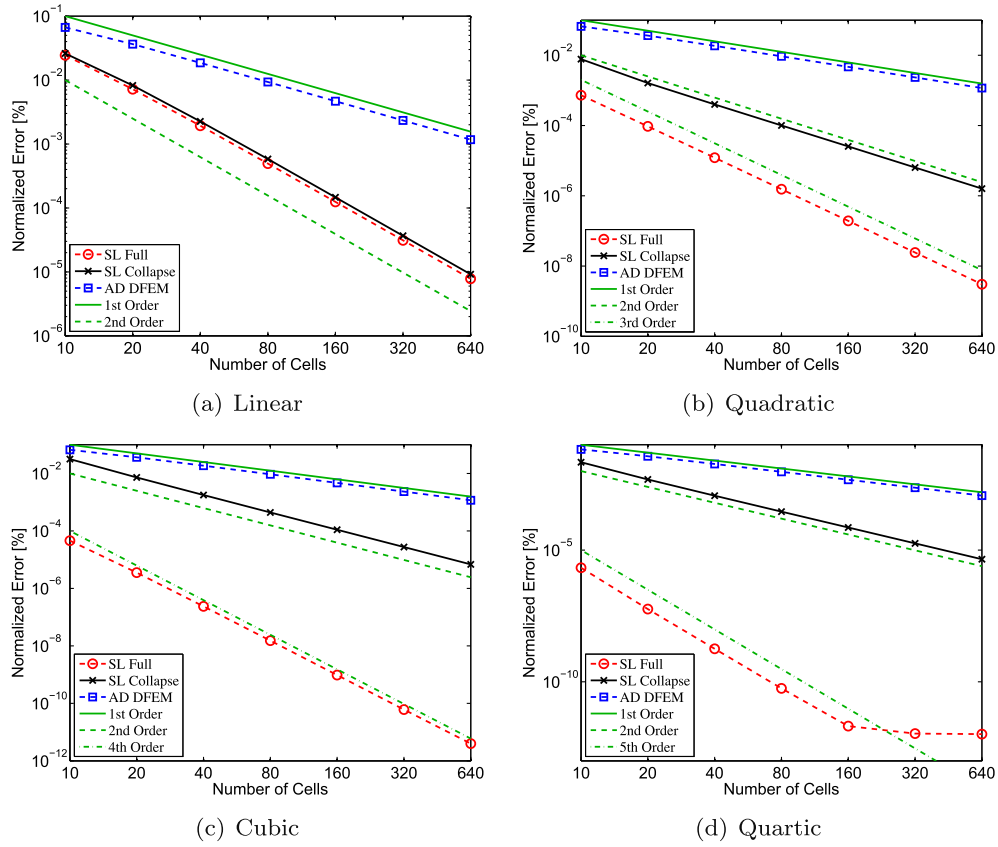


Fig. 19. Normalized fertile nuclide density, E_{N_f} , for the depletion problem at end of cycle, as a function of angular flux trial space degree.

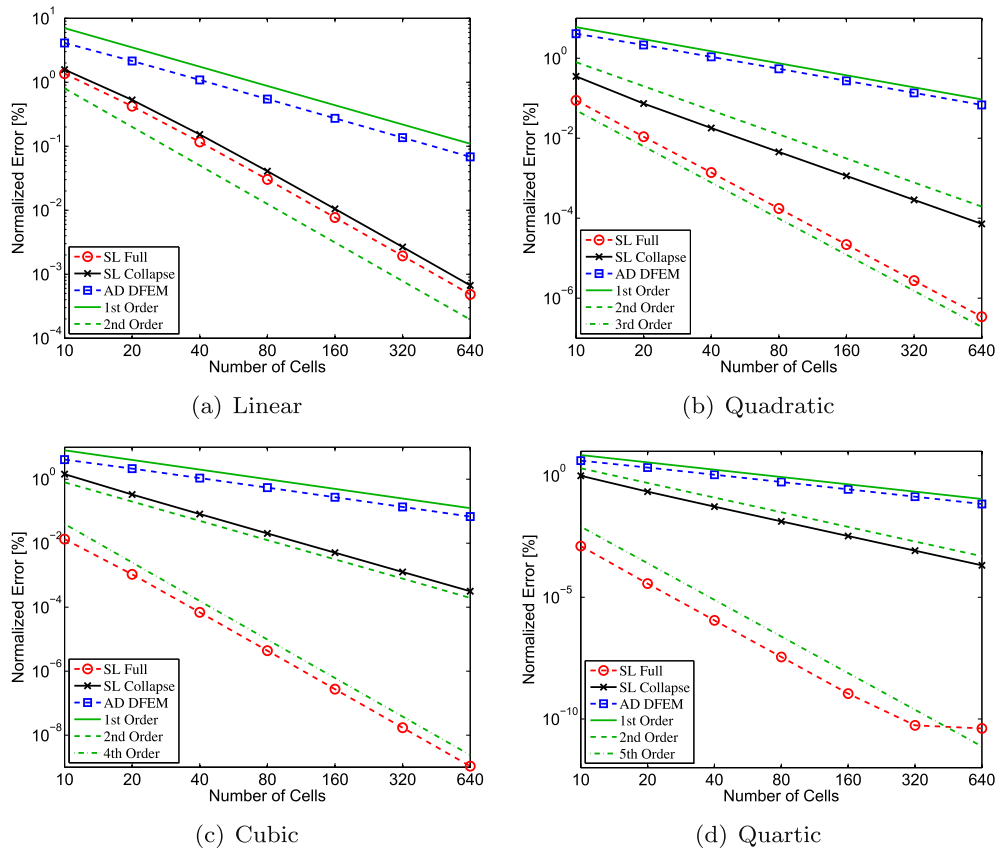


Fig. 20. Normalized parasitic absorber fission product error, $E_{N_{fpa}}$, for the depletion problem at end of cycle, as a function of angular flux trial space degree.

DFEM and SL Collapse scheme verifies the result observed in the pure absorber problem: assuming a cell-wise average cross section for coupled radiation transport problems limits the order of convergence of any quantity that depends on an interaction rate. SL Full achieves $P + 1$ order convergence of the error in spatial nuclide density for the fuel depletion problem, showing that coupled systems of equations involving radiation transport can be solved with arbitrary order of accuracy using high-order DFEM polynomial trial spaces and self-lumping numerical quadrature that explicitly accounts for the spatial variation of cross section within each cell.

6. Conclusions

We have presented several treatments to account for the effect of spatially varying cross sections with arbitrary-order discontinuous finite element (DFEM) approximations of the S_N radiation transport equations. Specifically, we have focused on so-called self-lumping numerical schemes. In an attempt to find robust, high-order accurate schemes, we considered self-lumping DFEM schemes that used (i) equally-spaces closed Newton–Cotes (SLXS Newton–Cotes), (ii) Lobatto (SLXS Lobatto), and (iii) Gauss (SLXS Gauss) quadratures as both the interpolation and quadrature points.

Only the SLXS Lobatto and SLXS Newton–Cotes schemes with a linear angular flux trial space resulted in strictly positive angular flux outflows, regardless of cross-section spatial variation or total cell optical thickness. For higher-order DFEM schemes, guaranteed robustness requires the use of cell-wise constant cross sections and self-lumping schemes, as outlined in Maginot et al. (2014). However, since schemes that assume cell-wise constant cross sections converge the angular flux with at most second-order accuracy, regardless of DFEM scheme and trial space degree, a decision must be made between solution accuracy and positivity.

The accuracy of self-lumping schemes was assessed by considering a pure absorber problem with a spatially varying cross section and a fuel depletion problem. Self-lumping schemes that used Lobatto or Gauss quadrature as the DFEM interpolation points and explicitly accounted for cross-section variation in space converged radiation fluxes with order $P + 1$, where P is the polynomial degree of the angular flux trial space.

In addition to the angular flux convergence, we also considered the accuracy of each scheme in calculating interaction rates. For the pure absorber problem, we demonstrated that assuming a cell-wise constant cross section results in highly non-physical, non-monotonic discontinuities in the DFEM approximation of the spatial interaction rate, which we referred to as blading. Regardless of whether a volume-averaged or flux-weighted cell-wise constant cross section was used, non-monotonic behavior in the point-wise interaction rate was observed. Additionally, convergence of the spatial interaction rate error is at most first order in space for any degree DFEM trial space scheme that assumes a cell-wise constant cross section when the true cross section varies within each cell. Self-lumping schemes using Gauss or Lobatto points as the DFEM interpolation points converge the spatial interaction rate with order $P + 1$ and their approximation of the interaction does not exhibit blading.

For the fuel depletion problem, convergence of spatial interaction rate was measured indirectly by measuring the spatial distribution of nuclide density during irradiation. The self-lumping scheme (SL Full) that expanded spatial nuclide density in a P degree DFEM trial space and explicitly accounted for the spatial variation of cross section converged the spatial nuclide density with order $P + 1$ in space. The SL Collapse scheme that expanded angular flux and nuclide density as P degree polynomials but did not account for the spatial variation of cross section converged

the spatial distribution of nuclides at most second order in space. Finally, the scheme that assumed a cell-wise average cross section and tracked only cell average nuclide density, AD DFEM, converged the spatial distribution of nuclide density at most first order in space, regardless of the angular flux trial space degree.

Future work will focus on the development of efficient solution acceleration techniques for high-order DFEM S_N transport methods that account for cross-section spatial dependence. Additionally, we wish to implement our self-lumping schemes in multiple spatial dimensions. Extension to 2-D quadrilaterals and 3-D hexahedral cells is straightforward with tensor product quadrature rules (Abramowitz and Stegun, 1972). Also, self-lumping schemes can be applied to triangular and tetrahedral grids using the various quadratures developed for these types of elements (Wandzura and Xiao, 2003; Liu and Vinokur, 1998). Whether the accuracy of self-lumping schemes observed for 1-D slabs can be replicated in multi-dimensional geometries is the topic of ongoing research.

Acknowledgment

Portions of this work were made possible by the support of the DOE CSGF program, provided under Department of Energy grant DE-FG02-97ER25308.

Appendix A. Influence of mesh spacing on solution accuracy

Two alternative meshing strategies are compared to equally-spaced meshed. In the following, we will use a shorthand notation, given in Table 2. With the MFP meshing strategy, we find each cell width by determining the width of each cell from $i = 1$ (leftmost cell) to $i = N_{cell}$ as outlined by Eq. (46): First, we determine the average cell optical thickness:

$$\bar{h} = \frac{\int_{x_{1/2}}^{x_{N_{cell}+1/2}} \Sigma_t(x) dx}{N_{cell}}. \quad (46a)$$

Then, we solve the following equation for $x_{i+1/2}$:

$$\int_{x_{i-1/2}}^{x_{i+1/2}} \Sigma_t(x) dx - \bar{h} = 0, \quad (46b)$$

yielding

$$x_{i+1/2} = \frac{1}{c_2} \log \left[\frac{c_2(\bar{h} + \Sigma_t(x_{i-1/2}))}{c_1} \right]. \quad (46c)$$

There are several ways to specify LOG spacing, but we elected to set a ratio, 0.6, between adjacent cell sizes with the caveat that we would set a minimum cell size, Δx_{min} . In our convergence testing, at the first refinement when $\Delta x_{N_{cell}} < \Delta x_{min}$, the grid is “fixed” and all further refinements uniformly refine the “fixed” grid. $\Delta x_{N_{cell}}$ is the cell width for the right most cell where, for $R < 1$,

$$\Delta x_i = \Delta x_1 R^{i-1}, \quad i \in [1, N_{cell}]. \quad (47)$$

Δx_1 is determined by requiring that the geometric series of cell widths completely fill the space:

$$\Delta x_1 = (x_{N_{cell}+1/2} - x_{1/2}) \frac{1 - R}{1 - R^{N_{cell}}} \quad (48)$$

The grid is “fixed” by resetting the width of every cell whose width, if set to the value required for a purely logarithmically spaced grid with R would be below Δx_{min} , to Δx_{min} . After imposing this, cell widths are determined by requiring the cells that were not reset to fill the problem space logarithmically using R . If there is no minimum cell width, at high mesh refinements, most cells will be infinitesimally small and the large cells will never be refined, causing error to stagnate. Logarithmic spacing represents the “smart”

meshing strategy most likely to be employed in engineering practice as it requires the least amount of solution information prior to problem execution. For all of our calculations, we set $R = 0.6$ and $\Delta x_{\min} = 10^{-3}$ [cm].

First, we note that the choice of mesh spacing method does not alter asymptotic convergence rates, as shown in Fig. 12. Fig. 12 shows that the SLXS Lobatto scheme with a quadratic trial space converges E_{ψ} , E_{ψ_A} , E_{IR} , and E_{IR_A} at the same asymptotic rate, regardless of grid spacing choice. Plots showing other trial space degrees and DFEM schemes are omitted for brevity. We also omit showing the convergence of $E_{\psi_{out}}$ as we have already demonstrated that the convergence rate of $E_{\psi_{out}}$ and E_{IR_A} are related and identical.

At mesh refinements that are not in the asymptotic convergence regime (low resolution grids), the selection of an alternate meshing methodology can result in a significant reduction in error. For instance, Fig. 13 shows the convergence for E_{ψ} , E_{ψ_A} , E_{IR} , and E_{IR_A} using the CXS DFEM scheme for a quadratic trial space. First, we note that any particular mesh spacing methodology results in solutions that are more accurate for certain quantities, but not for all quantities. We note that LOG spacing is more accurate in calculating interaction rate quantities (E_{IR} and E_{IR_A}) than an equally-spaced mesh. However, CXS DFEM shows a two order of magnitude reduction in calculating E_{IR_A} when using a mesh that has a uniform optical thickness in each cell. This is a direct result of CXS DFEM converging as $\delta\Delta x \rightarrow 0$.

Appendix B. Fuel depletion problem

The fuel depletion problem geometry is a 1-D layer of fuel and moderator regions as given in Fig. 14 of Section 5. Initially, each fuel region is a homogeneous mixture containing only fissile ^{235}U and fertile ^{238}U nuclei, with compositions given in Table 3. As fuel depletion progresses, the isotopic composition of fuel changes. The moderator is light water and its composition, given in Table 4, does not change with irradiation. We track five nuclide types in the fuel during the fuel depletion problem: fissile, fertile, parasitic absorber fission product, scattering fission product, and inert, whose spatial nuclide densities, [atom/cm³], are respectively denoted as N_{FS} , N_{FT} , N_{FP-A} , N_{FP-S} , and N_I .

We use a two-energy-group approximation with the standard numbering convention. All neutrons are born fast, there is no thermal upscattering, and we assume all scattering and fission is isotropic. Under these assumptions, and given the transmutation paths given in Fig. 15, the fully analytic, nonlinear depletion equations are:

$$\mu \frac{\partial \psi_1}{\partial x} + \Sigma_{t,1} \psi_1 = \frac{\Sigma_{s,1-1}}{2} \phi_1 + \frac{1}{k} \left(\frac{\nu \Sigma_{f,1}}{2} \phi_1 + \frac{\nu \Sigma_{f,2}}{2} \phi_2 \right) \quad (49a)$$

$$\mu \frac{\partial \psi_2}{\partial x} + \Sigma_{t,2} \psi_2 = \frac{\Sigma_{s,2-2}}{2} \phi_2 + \frac{\Sigma_{s,1-2}}{2} \phi_1 \quad (49b)$$

Table 3
Fuel atom density data.

Fuel density [g/cm ³]	10.97
Atom fraction ^{235}U	0.05
Atom fraction ^{238}U	0.95
Fuel molecular weight [amu]	270.03

Table 4
Water atom density data.

Water density [g/cm ³]	1
Atom fraction ^1H	$\frac{2}{3}$
Atom fraction ^{16}O	$\frac{1}{4}$
Water molecular weight [amu]	18.02

$$\begin{aligned} \frac{\partial N_{FS}}{\partial t} = & -N_{FS} \left[(1 - \gamma_{FS,1}) \sigma_{a,FS,1} \phi_1 + (1 - \gamma_{FS,2}) \sigma_{a,FS,2} \phi_2 \right] \\ & + N_{FT} [\gamma_{FT,1} \sigma_{a,FT,1} \phi_1 + \gamma_{FT,2} \sigma_{a,FT,2} \phi_2] \end{aligned} \quad (49c)$$

$$\frac{\partial N_{FT}}{\partial t} = -N_{FT} [\sigma_{a,FT,1} \phi_1 + \sigma_{a,FT,2} \phi_2] \quad (49d)$$

$$\begin{aligned} \frac{\partial N_{FP-S}}{\partial t} = & N_{FS} [(1 - p_{FS,1}) \gamma_{FS,1} \sigma_{a,FS,1} \phi_1 + (1 - p_{FS,2}) \gamma_{FS,2} \sigma_{a,FS,2} \phi_2] \\ & + N_{FT} [(1 - p_{FT,1}) \gamma_{FT,1} \sigma_{a,FT,1} \phi_1] - N_{FS} [\sigma_{a,FP-S,1} \phi_1 + \sigma_{a,FP-S,2} \phi_2] \end{aligned} \quad (49e)$$

$$\begin{aligned} \frac{\partial N_{FP-A}}{\partial t} = & N_{FS} [p_{FS,1} \gamma_{FS,1} \sigma_{a,FS,1} \phi_1 + p_{FS,2} \gamma_{FS,2} \sigma_{a,FS,2} \phi_2] \\ & + N_{FT} p_{FT,1} \gamma_{FT,1} \sigma_{a,FT,1} \phi_1 \\ & - N_{FP-A} [(1 - \xi_{FP-A,1}) \sigma_{a,FP-A,1} \phi_1 + (1 - \xi_{FP-A,2}) \sigma_{a,FP-A,2} \phi_2] \end{aligned} \quad (49f)$$

$$\begin{aligned} \frac{\partial N_I}{\partial t} = & N_{FP-A} [\xi_{FP-A,1} \sigma_{a,FP-A,1} \phi_1 + \xi_{FP-A,2} \sigma_{a,FP-A,2} \phi_2] \\ & + N_{FP-S} [\sigma_{a,FP-S,1} \phi_1 + \sigma_{a,FP-S,2} \phi_2]. \end{aligned} \quad (49g)$$

In Eqs. (49a) and (49b) ϕ_g is the group g scalar flux [n/cm²/sec], $\Sigma_{t,g}$ is the total macroscopic cross section [cm⁻¹] of group g , $\Sigma_{s,g \rightarrow g'}$ [cm⁻¹] is the macroscopic cross section for neutrons scattering from group g to group g' , k is the system multiplication factor, and $\nu \Sigma_{f,g}$ is the average number of neutrons released per fission (ν) for a fission induced by a neutron in group g , multiplied by the group g macroscopic fission cross section. We use Gauss–Legendre S_2 angular quadrature, with weights that sum to 2, to approximate the scalar fluxes.

The nuclide production destruction equations, Eqs. (49c)–(49g), use the following notation: $\gamma_{m,g}$ is the probability that a neutron absorption in nuclide m results in the production of a fissile isotope, $y_{m,g}$ is the ratio of nuclide m 's fission cross section to total cross section for group g , $p_{m,g}$ is the probability that the fission of nuclide m yields a parasitic absorber fission product, and ξ_g is the probability that when a parasitic absorber fission production absorbs a neutron, another parasitic absorber fission product is produced. Though not explicitly noted in Eqs. (49), all scalar fluxes ϕ_g , macroscopic cross sections Σ_g , and nuclide densities N , are functions of position.

Eqs. (49) are solved using a semi-static approach (Bell and Glasstone, 1970) assuming the flux distribution at the start of the time step remains constant throughout the time step. Nuclide densities are advanced in time using explicit Euler time differencing.

We consider three numerical schemes for the fuel depletion problem:

1. AD DFEM: expands the angular flux in a P degree polynomial trial space using equally-spaced interpolation points, uses exact spatial integration, assumes cell-wise constant cross sections for solving the radiation equations, and tracks only cell average nuclide densities.
2. SL Collapse: expands both the angular flux and nuclide densities in a P degree polynomial trial space, uses self-lumping quadrature to approximate integrals, and assumes cell-wise constant cross sections for solving the radiation equations. Lobatto quadrature is used as the DFEM interpolation points for odd degree trial spaces and Gauss quadrature as the DFEM interpolation points for even degree trial spaces.
3. SL Full: expands both the angular flux and nuclide densities in a P degree polynomial trial space, uses self-lumping quadrature to approximate integrals, and explicitly accounts for the variation of macroscopic cross section within each spatial cell. Lobatto quadrature is used as the DFEM interpolation points for odd

degree trial spaces and Gauss quadrature as the DFEM interpolation points for even degree trial spaces.

B.1. Radiation solution technique

The spatially discretized radiation equations are:

$$\mu_d \mathbf{L} \vec{\psi}_{d,1} - \mu_d \psi_{in,d,1} \vec{f} + \frac{\Delta x}{2} \mathbf{R}_{\Sigma_{t,1}} \vec{\psi}_{d,1} = \frac{\Delta x}{4} \mathbf{R}_{\Sigma_{s,1-1}} \vec{\phi}_1 + \frac{1}{k_\tau} \frac{\Delta x}{4} (\mathbf{R}_{\Sigma_{f,1}} \vec{\phi}_1 + \mathbf{R}_{\Sigma_{f,2}} \vec{\phi}_2), \quad (50)$$

and

$$\mu_d \mathbf{L} \vec{\psi}_{d,2} - \mu_d \psi_{in,d,2} \vec{f} + \frac{\Delta x}{2} \mathbf{R}_{\Sigma_{t,2}} \vec{\psi}_{d,2} = \frac{\Delta x}{4} (\mathbf{R}_{\Sigma_{s,2-2}} \vec{\phi}_2 + \mathbf{R}_{\Sigma_{s,1-2}} \vec{\phi}_1). \quad (51)$$

In Eq. (50) and Eq. (51) k_τ is the multiplication factor at time index τ and $\mathbf{R}_{\Sigma_{s,1-1}}$, $\mathbf{R}_{\Sigma_{s,1-2}}$, $\mathbf{R}_{\Sigma_{s,2-2}}$, $\mathbf{R}_{\Sigma_{f,1}}$, and $\mathbf{R}_{\Sigma_{f,2}}$ are defined analogously to \mathbf{R}_{Σ_t} , as in Eq. (15), replacing $\Sigma_t(s)$ with $\Sigma_{s,1-1}(s)$, $\Sigma_{s,1-2}(s)$, $\Sigma_{s,2-2}(s)$, $\Sigma_{f,1}(s)$, and $\Sigma_{f,2}(s)$, respectively.

The AD DFEM and SL Collapse scheme approximate the various \mathbf{R} matrices by using a cell-wise average cross section, as in Eq. (21). While AD DFEM uses the exact mass matrix, as defined in Eq. (16), SL Collapse approximates \mathbf{M} as in Eq. (23b). However, given we use Gauss quadrature as the DFEM interpolation points for even degree trial spaces and Lobatto quadrature for odd degree trial spaces, the SL Collapse mass matrix is exact for even degree polynomial trial spaces and inexact for odd degree trial spaces. The SL Full scheme approximates the various \mathbf{R} as in Eq. (23a).

We solve Eqs. (50) and (51) following the standard power iteration procedure, described for DFEM radiation transport in Warsa et al. (2004). Convergence is checked after each power iteration. Using ℓ as the iteration index, convergence after the $\ell + 1$ iterate is said to occur when:

$$\delta_k = \left| \frac{k^{(\ell+1)} - k^{(\ell)}}{k^{(\ell)}} \right| < \epsilon_k, \quad (52)$$

and

$$\delta_\phi = \max_{g=1,2} \max_{i=1,\dots,N_{cell}} \max_{j=1,\dots,N_p} \left| \frac{\phi_{g,i,j}^{(\ell+1)} - \phi_{g,i,j}^{(\ell)}}{\phi_{g,i,j}^{(\ell)}} \right| < \epsilon_\phi. \quad (53)$$

In our computational results we use $\epsilon_k = 10^{-12}$ and $\epsilon_\phi = 10^{-10}$. For each power iteration, the within group components of Eqs. (50) and (51) are solved using transport sweeps (Lewis and Miller, 1993) and S_2 synthetic acceleration (S2SA) (Lorence et al., 1989).

The converged scalar flux is normalized such that the desired power level of $P_{Total} = 2000$ [W/cm²], is achieved. For the SL Full scheme, we calculate the normalization factor, F_p , as:

$$F_p = E_f \sum_{g=1}^2 \left[\sum_{i=1}^{N_{Fuel}} \frac{\Delta x_i}{2} \sum_{j=1}^{N_p} w_j \Sigma_{f,g,i,j} \phi_{g,i,j} \right], \quad (54)$$

where in E_f is the energy released per fission, assumed to be 200 [MeV], w_j is the quadrature weight associated with the j -th DFEM interpolation point, and N_{Fuel} is the total number of spatial cells in the fuel region. All fission energy is assumed to be deposited only in the fuel. The SL Collapse and AD DFEM schemes calculate F_p as

$$F_p = E_f \sum_{g=1}^2 \left[\sum_{i=1}^{N_{Fuel}} \frac{\Delta x_i}{2} \sum_{j=1}^{N_p} w_j \Sigma_{f,g,i,j} \phi_{g,i,j} \right]. \quad (55)$$

$\tilde{\phi}^{(\ell+1)}$ is then scaled as:

$$\tilde{\phi}_g^{(\ell+1)} \leftarrow \frac{P_{Total}}{F_p} \tilde{\phi}_g^{(\ell+1)}. \quad (56)$$

B.2. Nuclide spatial discretization

We consider three spatial discretization schemes to solve the nuclide production/destruction components of Eq. (49). The first, AD DFEM, tracks only cell average nuclide densities, approximating the true spatial distribution of nuclide m , $N_m(x, t)$, as being a constant in each cell, equal to the cell average density of nuclide m . Denoting the average nuclide density in cell i for nuclide m as $\bar{N}_{m,i}$ and the average group g scalar flux in cell i as $\bar{\phi}_{g,i}$, we give the fissile nuclide update equation for the AD DFEM scheme in Eq. (57):

$$\frac{\bar{N}_{FS,i}^{\tau+1} - \bar{N}_{FS,i}^\tau}{\Delta t} = \bar{N}_{FT,i}^\tau \left[\gamma_{FT,1} \sigma_{a,FT,1} \bar{\phi}_{1,i}^\tau + \gamma_{FT,2} \sigma_{a,FT,2} \bar{\phi}_{2,i}^\tau \right] - \bar{N}_{FS,i}^\tau \left((1 - \gamma_{FS,1}) \sigma_{a,FS,1} \bar{\phi}_{1,i}^\tau + (1 - \gamma_{FS,2}) \sigma_{a,FS,2} \bar{\phi}_{2,i}^\tau \right). \quad (57)$$

In Eq. (57) superscript τ denotes time index τ quantities and Δt is the time step size. The update equations for N_{FT} , N_{FP-A} , N_{FP-S} , and N_I can be derived analogously to Eq. (57). AD DFEM calculates $\bar{\phi}_{g,i}$ using closed Newton–Cotes quadrature with the quadrature points limited to the DFEM interpolation points:

$$\bar{\phi}_{g,i} = \frac{1}{2} \sum_{j=1}^{N_p} w_j \phi_{g,i,j}. \quad (58)$$

The averaging in Eq. (58) is exact since an N_p point closed Newton–Cotes quadrature can exactly integrate any P degree polynomial. Eq. (57) locally updates $\bar{N}_{FS,i}$ via a 5×5 matrix–vector multiply.

The SL Full and SL Collapse schemes approximate the true spatial density of nuclide m as a P degree Lagrange polynomial, $\tilde{N}_m(s)$, in each cell:

$$\tilde{N}_m(s) = \sum_{j=1}^{N_p} N_{mj} B_j(s), \quad (59)$$

where B_j are the $N_p = P + 1$ Lagrange interpolatory polynomials in the interval $s \in [-1, 1]$. We require the set of nuclide density DFEM interpolation points to be the same set of N_p points as the angular flux DFEM interpolation points. Following a Galerkin procedure, we multiply each production/destruction nuclide equation in Eq. (49) by basis function B_j and integrate generating a $5(P + 1) \times 5(P + 1)$ system of equations. The system of update equations for $\tilde{N}_{FS,i}$ is shown in Eq. (60):

$$\frac{1}{\Delta t} \frac{\Delta x}{2} \mathbf{M} (\tilde{N}_{FS,i}^{\tau+1} - \tilde{N}_{FS,i}^\tau) = - (1 - \gamma_{FS,1}) \sigma_{a,FS,1} \frac{\Delta x}{2} \widehat{\mathbf{M}}_{\phi_{1,i},\tau} \tilde{N}_{FS,i}^\tau - (1 - \gamma_{FS,2}) \sigma_{a,FS,2} \frac{\Delta x}{2} \widehat{\mathbf{M}}_{\phi_{2,i},\tau} \tilde{N}_{FS,i}^\tau + \gamma_{FT,1} \sigma_{a,FT,1} \frac{\Delta x}{2} \widehat{\mathbf{M}}_{\phi_{1,i}^\tau} \tilde{N}_{FT,i}^\tau + \gamma_{FT,2} \sigma_{a,FT,2} \frac{\Delta x}{2} \widehat{\mathbf{M}}_{\phi_{2,i}^\tau} \tilde{N}_{FT,i}^\tau. \quad (60)$$

Table 5

Water microscopic cross section. Assumed that water is composed only of H₂O. All cross sections given in barns [10^{-24} cm²].

Nuclide	$\sigma_{a,1}$	$\sigma_{a,2}$	$\sigma_{s,1-1}$	$\sigma_{s,2-2}$	$\sigma_{s,1-2}$
¹ H	0	0.332	0	20.47	3.926
¹⁶ O	0	0	2.739	3.780	0

Table 6

Fuel microscopic cross sections. All cross sections given in barns [10^{-24} cm²].

Nuclide	$\sigma_{a,1}$	$\sigma_{a,2}$	$\sigma_{s,1-1}$	$\sigma_{s,2-2}$	$\sigma_{s,1-2}$
²³⁵ U	1.325	683.21	4.566	15.04	0
²³⁸ U	0.374	2.717	4.804	9.36	0

Table 7Fission cross section data in barns [10^{-24} cm²], radiative capture fraction, and fission probability for fissile and fertile nuclides.

Nuclide	ν_1	ν_2	$\sigma_{f,1}$	$\sigma_{f,2}$	γ_1	γ_2	y_1	y_2
$^{235}_{92}\text{U}$	2.6	2.4	1.235	584.4	$\frac{0.09}{1.325} = 0.068$	$\frac{98.81}{683.21} = 0.145$	$\frac{1.235}{1.325} = 0.932$	$\frac{584.4}{683.21} = 0.855$
$^{238}_{92}\text{U}$	2.8	N/A	0.308	0	$\frac{0.066}{0.374} = 0.177$	1	$\frac{0.308}{0.374} = 0.823$	0

Table 8Parasitic absorber fission product, scattering fission product, and inert nuclide microscopic cross section data. All cross sections given in barns [10^{-24} cm²].

Nuclide	$\sigma_{a,1}$	$\sigma_{a,2}$	$\sigma_{s,1}$	$\sigma_{s,2}$	$\sigma_{s,1-2}$
FP-A	15	1000	0.5	5	0
FP-S	0.5	5	15	100	0
Inert	1	5	1	5	0

Table 9

Fission product branch ratios and parasitic absorber fission product regeneration fraction.

$p_{FS,1}$	0.3
$p_{FS,2}$	0.3
$p_{FT,1}$	0.3
$p_{FT,2}$	0.3
$\xi_{FP-A,1}$	0.3
$\xi_{FP-A,2}$	0.5

The equations for $\tilde{N}_{FT,i}$, $\tilde{N}_{FP-A,i}$, $N_{FP-S,i}$, and $N_{I,i}$ are derived in a similar fashion to Eq. (60). In Eq. (60) we have defined:

$$\widehat{\mathbf{M}}_{\phi_g^{\tau,jk}} = \int_{-1}^1 B_j(s) B_k(s) \tilde{\phi}_{g,\tau,i}(s) ds, \text{ and} \quad (61)$$

$$\tilde{\mathbf{N}}_{m,i}^{\tau} = \begin{bmatrix} N_{m,1}^{\tau} \\ \vdots \\ N_{m,j}^{\tau} \\ \vdots \\ N_{m,P+1}^{\tau} \end{bmatrix}. \quad (62)$$

Given that we track five nuclides in the fuel region, each expanded in a P degree polynomial in each cell, there are $5(P+1)$ unknowns in each cell, thus Eq. (60) is a closed, $5(P+1) \times 5(P+1)$ system of linear equations for the $5(P+1)$ unknown $N_{FS,i,j}$ in each cell.

Using self-lumping quadrature to approximate Eq. (61) causes $\widehat{\mathbf{M}}_{\phi_g^{\tau,jk}}$ to be a diagonal matrix. Recalling that \tilde{N}_m uses the same interpolation points as $\tilde{\phi}_g$, approximating the integration of Eq. (61) with numerical quadrature restricted to the DFEM interpolating points, results in

$$\widehat{\mathbf{M}}_{\phi_g^{\tau,jk}} = \begin{cases} w_j \phi_{g,\tau,i,j} & j = k \\ 0 & \text{otherwise} \end{cases}. \quad (63)$$

Macroscopic cross sections are generated from nuclide density and microscopic cross section data. For the AD DFEM scheme, each cell has a single macroscopic cross section (per reaction type), and a single value of nuclide density for each nuclide type. Thus, interaction cross sections are easily tabulated. As an example, $\Sigma_{t,g}$ in cell i is shown in Eq. (64):

$$\hat{\Sigma}_{t,g,i} = N_{FS,i} \sigma_{t,FS,g} + N_{FT,i} \sigma_{t,FT,g} + N_{FP-A,i} \sigma_{t,FP-A,g} + N_{FP-S,i} \sigma_{t,FP-S,g} + N_{I,i} \sigma_{t,I,g}. \quad (64)$$

Macroscopic fission cross section and average neutrons per fission products are found in a similar fashion, but we can limit our

consideration to the fissile and fertile nuclide densities as shown in Eq. (65),

$$\widehat{\nu \Sigma}_{f,g,i} = N_{FS,i} \nu_{FS,g} \sigma_{f,FS,g} + N_{FT,i} \nu_{FT,g} \sigma_{f,FT,g}. \quad (65)$$

The SL Full and SL Collapse schemes calculate macroscopic cross sections in a similar fashion to Eqs. (64) and (65), but instead of calculating a cell average, $\hat{\Sigma}_{g,i}$, they calculate macroscopic values at each DFEM interpolation point. SL Collapse then averages the macroscopic cross section at each DFEM interpolation point to estimate the cell average cross section, as shown in Eq. (66) for $\hat{\Sigma}_{t,i}$:

$$\hat{\Sigma}_{t,i} = \frac{1}{2} \sum_{j=1}^{N_p} w_j \Sigma_{t,g,i,j}. \quad (66)$$

B.3. Physical Data

We complete the specification of the depletion problem by giving the physical data used to solve the problem. Microscopic cross section data for the water is given in Table 5. Absorption and scattering cross sections for the fertile and fissile nuclides are given in Table 6, and fission cross sections and average neutrons per fission are given in Table 7. Cross-section data for the fission products and inert nuclides are given in Table 8. Fission product yields and the parasitic absorber fission product regeneration fraction, ξ , are given in Table 9.

References

- Abramowitz, M., Stegun, I.A., 1972. Handbook of Mathematical Functions with Formulas, Graphs, and Mathematical Tables. United States Department of Commerce, Washington, DC.
- Adams, M.L., 1997. Subcell balance methods for radiative transfer on arbitrary grids. Transport Theory Stat. Phys. 26 (4&5), 385–431.
- Adams, M.L., 2001. Discontinuous finite element transport solutions in thick diffusive problems. Nucl. Sci. Eng. 137, 298–333.
- Adams, M.L., Nowak, P.F., 1998. Asymptotic analysis of a computational method for time- and frequency-dependent radiative transfer. J. Comput. Phys. 146, 366–403.
- Adams, M.P., et al. 2013. Provably optimal parallel transport sweeps on regular grids. In: International Conference on Mathematics and Computational Methods Applied to Nuclear Science and Engineering (M&C 2013), Sun Valley, ID, 5–9 May, 2013.
- Bell, G., Glasstone, S., 1970. Nuclear Reactor Theory. Van Nostrand Reinhold, Inc., New York, NY.
- Kavenoky, A., Lautard, J., 1977. A finite element depletion diffusion calculation method with space-dependent cross section. Nucl. Sci. Eng. 64 (2), 563–575.
- Lewis, E.E., Miller, W.F., 1993. Computational Methods of Neutron Transport. American Nuclear Society, La Grange Park, IL.
- Liu, Y., Vinokur, M., 1998. Exact integrations of polynomials and symmetric quadrature formulas over arbitrary polyhedral grids. J. Comput. Phys. 140, 122–147.
- Lorence, L.J., Morel, J.E., Larsen, E.W., 1989. An S_2 synthetic acceleration scheme for the one-dimensional S_N equations with linear discontinuous spatial differencing. Nucl. Sci. Eng. 101, 341–351.
- Maginot, P.G., Ragusa, J.C., Morel, J.E., 2014. Lumping techniques for DFEM S_N transport in slab geometry. Nucl. Sci. Eng. (accepted for publication).
- McGraw, C.N., et al., 2014. Accuracy of the linear discontinuous Galerkin method for reactor analysis with resolved fuel pins. In: The Role of Reactor Physics Toward a Sustainable Future (PHYSOR 2014), Kyoto, Japan, September 28–October 3, 2014.
- Morel, J.E., Wareing, T.A., Smith, K., 1996. A linear-discontinuous spatial differencing scheme for S_N radiative transfer. J. Comput. Phys. 4, 475–498.
- Morel, J.E., Yand, T.-Y.B., Warsa, J.S., 2007. Linear multifrequency-grey acceleration recast for preconditioned Krylov iterations. J. Comput. Phys. 227, 244–264.
- Ober, C.C., Shadid, J.N., 2004. Studies on the accuracy of time-integration methods for the radiation-diffusion equations. J. Comput. Phys. 195, 743–772.

- Raviart, P.A., 1972. The use of numerical integration in finite element methods for solving parabolic equations. In: Conference on Numerical Analysis, RIANA 1972, Dublin, Ireland, 14–18 August, pp. 233–264.
- Santandrea, S., Bellier, P., 2007. An unstructured characteristics scheme with a linear expansion for both fluxes and cross sections. In: Proceedings of the Joint International Topical Meeting on Mathematics & Computation and Supercomputing in Nuclear Applications (M&C + SNA 2007), Monterey, California.
- Stacey, W.M., 2001. *Nuclear Reactor Physics*. John-Wiley & Sons Inc., New York, NY.
- Thomee, V., 1997. *Galerkin Finite Element Methods for Parabolic Problems*. Springer, New York.
- Wandzura, S., Xiao, H., 2003. Symmetric quadrature rules on a triangle. *Comput. Math. Appl.* 45, 1829–1840.
- Wang, Y., Ragusa, J.C., 2009. A high-order discontinuous Galerkin method for the S_N transport equations on 2D unstructured triangular meshes. *Ann. Nucl. Energy* 36, 931–939.
- Warsa, J.S., Wareing, T.A., Morel, J.E., McGhee, J.M., Lehoucq, R.B., 2004. Krylov subspace iterations for deterministic k -eigenvalue calculations. *Nucl. Sci. Eng.* 147, 26–42.
- Warsa, J.S., Wareing, T.A., Morel, J.E., 2004. Krylov iterative methods and the degraded effectiveness of diffusion synthetic acceleration for multidimensional S_N calculations in problems with material discontinuities. *Nucl. Sci. Eng.* 147 (3), 218–248.